GSA Data Repository 2018075

Shi et al., 2018, Sulfur isotope evidence for transient marine-shelf oxidation during the Ediacaran Shuram Excursion: Geology, https://doi.org/10.1130/G39663.1.

Geological Setting

The Doushantuo Formation was deposited on the South China Craton, a microcontinent thought to have been located at low Northern Hemisphere paleolatitudes (Fig. DR1A; Zhang et al., 2015), immediately after the last Neoproterozoic global-scale glaciation—the Marinoan (or 'Nantuo' in South China) Glaciation. This formation exhibits inner-shelf facies to the northwest and basinal facies to the southeast of the Yangtze Platform (Fig. DR1B-C). The Yangtze Platform was probably a rimmed platform during deposition of middle Doushantuo Formation, but there is no evidence for water-mass restriction of the South China Basin (Jiang et al., 2011). Yet new paleomagnetic evidence suggest that South China was most likely an isolated continental block during the Ediacaran and early Cambrian (Zhang et al., 2015), well connected with open-ocean all around.

The depositional interval of the Doushantuo Formation is constrained by zircon U-Pb ages of 635.2±0.6 Ma and 551.1±0.7 Ma from ash beds at its base and top (Condon et al., 2005; Zhang et al., 2005), yielding a duration of ~84 million years (Myr) representing most of the Ediacaran Period. The Doushantuo Formation, which overlies the Cryogenian Nantuo Formation and underlies the upper Ediacaran Dengying Formation, is subdivided into four

lithostratigraphic members (Members I-IV) (Ding et al., 1996; Zhu et al., 2003). No evidence for significant erosional hiatuses within the formation has been reported, although small-scale unconformities in sedimentation may exist. Three transgressive-regressive (T-R) cycles are present in the Doushantuo and lower Dengying formations in their type area of the Yangtze Gorges. Cycle 1 begins with a transgression recorded by the basal cap carbonate overlain by deep subtidal shales/silty dolostone that exhibit parallel and wrinkle laminations (lower Member II), followed by a regression recorded by a shift to shallow subtidal carbonates with small-scale cross-lamination and phosphatic intraclasts (upper Member II). Cycle 2 begins above a sequence boundary near the Member II/III contact, with the transgressive phase recorded by laminated black shale and lime mudstones (lower Member III) and the regressive phase by phosphatic packstone exhibiting scour marks, low-angle cross-laminations, and microbial mats (upper Member III). Cycle 3 begins above another sequence boundary at the Member III/IV contact, with the transgressive phase recorded by deep subtidal black shales (Member IV) and the regressive phase by peritidal dolostones exhibiting tepee structures and karstification features (lower Dengying Formation) (Jiang et al., 2011; Zhu et al., 2003). The Doushantuo Formation is also famous for its fossil animal embryos (Yin et al., 2007), macroscopic algae (Yuan et al., 2011), and abundant acritarchs, all of which are milestones in the evolution of multicellular life (see Xiao et al., 2014).

The carbonate carbon isotope chemostratigraphy of the Doushantuo Formation, which exhibits considerable variation in $\delta^{13}C_{carb}$ values, has been reviewed in Jiang et al. (2007,2010), Zhou and Xiao (2007), Zhu et al. (2007), Ader et al. (2009), Wang et al. (2016),

and Li et al. (2017). Shallow-water, carbonate-rich sections in the Yangtze Gorges area are considered the most likely to have recorded a global $\delta^{13}C_{carb}$ signature. In this area, three major negative $\delta^{13}C_{carb}$ excursions, one each in the basal cap carbonate [Ediacaran Negative excursion 1 (EN1) or CAp carbonate Negative Carbon isotope Excursion (CANCE)], the middle [EN2 or BAIguoyuan Negative Carbon isotope Excursion (BAINCE)], and the upper Doushantuo Formation [EN3 or DOUshantuo Negative Carbon isotope Excursion (DOUNCE)], have been documented. These three negative excursions are separated by two Ediacaran Positive intervals (EP1 and EP2 in an ascending order) with $\delta^{13}C_{carb}$ values of ~+5‰. However, the magnitude of the EN2 excursion varies among sections in the Yangtze Gorges area, and its global significance remains uncertain. In contrast, EN1 and EN3 have well-established correlative features in India (Jiang et al., 2002; Kaufman et al., 2006), Oman (Fike et al., 2006; Le Guerroué et al., 2006; Le Guerroué and Cozzi, 2010), and Australia (Calver, 2000; Walter et al., 2000) and, with lesser certainty, in Namibia (Saylor et al., 1998; Halverson et al., 2005) and the western United States (Kaufman et al., 2007).

The Shuram Excursion (SE) represents the EN3/DOUNCE event, i.e., the uppermost of the three $\delta^{13}C_{carb}$ anomalies of the Doushantuo Formation (Zhu et al., 2007; McFadden et al., 2008). It is characterized in the Three Gorges area by a ~15 ‰ negative shift from ca. +5 ‰ to –10 ‰. The stratigraphic interval of the SE exhibits a distinctive succession of lithologies, including dolostone and bedded chert passing upsection into limestone-dolostone rhythmites in Member III, overlain by a ~10-m-thick black, organic-rich shale with calcite concretions in Member IV (McFadden et al., 2008; An et al.,

2015). In deep-water facies across the Yangtze Platform, the boundary between the Doushantuo Formation and the overlying Dengying or Liuchapo Formation is marked by a lithologic transition to characteristic chert (Jiang et al., 2007, 2011; Lu et al., 2013).

Within this sequence stratigraphic framework, the age of the SE can be roughly constrained by three chronological anchor points (Fig. 1): (1) ~551 Ma, a zircon U-Pb age from an ash bed ~85 cm below the top of the Member IV (black shales) in the Jiuqunao section, located ~20 km northwest of the Jiulongwan section (Condon et al., 2005). This age constrains the termination of the SE/EN3/DOUNCE event (e.g., Condon et al., 2005; Zhang et al., 2005; Jiang et al., 2007; Zhou and Xiao, 2007; Zhu et al., 2007; McFadden et al., 2008; Li et al., 2010, 2015; Sawaki et al., 2010; Lu et al., 2013; Kendall et al., 2015; Sahoo et al., 2016; Xiao et al., 2016; Zhou et al., 2017), although some uncertainties in regional stratigraphic correlation exist (e.g., An et al., 2015). (2) ~560 Ma, which corresponds to the base of the black shale unit (Member IV) of the uppermost Doushantuo Formation, an age from comprehensive stratigraphic correlation and estimates from Ediacaran Doushantuo age model (Kendall et al., 2015; Li et al., 2015). Given the zircon U–Pb ages of 635.2±0.6 Ma, 632.5±0.5 Ma, and 551.1±0.7 Ma from the base and top of the Doushantuo Formation (Condon et al., 2005), a simple age interpolation (cf. Saylor et al., 1998; Halverson et al., 2005) yields estimated ages for the two post-cap carbonate negative $\delta^{13}C$ anomalies of ~595-587 Ma (EN2/BAINCE) and ~575-551 Ma (EN3/DOUNCE) (Jiang et al., 2007) and for the base of Member IV of ~560 Ma (Jiang et al., 2007; Kendall et al., 2015). These estimates are consistent with a Pb–Pb age of 576±14 Ma from the upper phosphorite layers

of the Doushantuo Formation at Weng'an (Chen et al., 2004), which can be correlated to Member III of the Doushantuo Formation in the Three Gorges area based on the similarity of acritarch fossils between the Jiulongwan and Weng'an sections (e.g., Zhou et al., 2007; Xiao et al., 2014). Furthermore, these estimates are consistent with the occurrence of *Eoandromeda Octobrachiata* (Miaohe Biota) in the lower black shale, which is also found in the ~560-Ma Ediacara Member of the Rawnsley Quartzite of South Australia (cf. Zhu et al., 2008). (3) ~575 Ma, a rough age estimate for the base of the EP2. Stratigraphic analyses and Sr isotope data suggest that the SE is younger than the ~580-Ma Gaskiers Glaciation in South China (Sawaki et al., 2010), which has been correlated to a stratigraphic break (i.e., EN2) located immediately below EP2 in the Doushantuo Formation (Condon et al., 2005). This arrangement is also consistent with the linear interpolation based on available Doushantuo U-Pb ages, which suggests an age of ~595-587 Ma for the EN2 and an age of ~575-551 Ma for the SE/EN3/DOUNCE (Jiang et al., 2007). Therefore, the onset date of the SE, as recorded by the Doushantuo Formation, can be roughly placed at 575 Ma.

Study Sections

Jiulongwan (JLW; 30°47′51″N, 110°59′32″E) and Sidouping (SDP: 28°55′01″N, 110°27′00″E) are outcrop sections in Hubei Province and Hunan Province (South China), respectively. They represent an inner-shelf and an upper-slope setting, respectively, providing a representative proximal-to-distal transect across the Yangtze Platform (Fig. DR1B-C; Zhu et al., 2013). These sections contain ample carbonates in strata recording the

SE, allowing us to measure both $\delta^{13}C_{carb}$ and $\delta^{34}S_{CAS}$ and, thus, to investigate spatial variation in C-S cycling and its possible relationship to continental weathering fluxes (Jiang et al., 2010; Li et al., 2017).

At JLW, Member I corresponds to a ~5-m-thick cap carbonate exhibiting distinctive sedimentary structures/textures and negative $\delta^{13}C_{carb}$ values (EN1; Jiang et al., 2003, 2006). Member II consists of alternating organic-rich black shale and thinly bedded dolostone with phosphatic chert nodules, from which abundant acanthomorphic acritarchs have been reported (Zhou et al., 2007; McFadden et al., 2008, 2009; Liu et al., 2013). Member III, which contains the peak negative $\delta^{13}C$ excursion (EN3), consists of ~70 m of thin- to thick-bedded dolostone and limestone (Jiang et al., 2007; Zhou and Xiao, 2007; McFadden et al., 2008; Lu et al., 2013). Member IV comprises a ~10-m-thick organic-rich black shale unit directly underlying the Dengying Formation (Jiang et al., 2007; McFaddden et al., 2008, Li et al., 2010, 2017). At SDP, the section consists mainly of cap carbonate, thinly-bedded black shale, and laminated microcrystalline limestone, and cherty dolostone, and shaly dolostone with abundant syndepositional folds, slump blocks, and olistostrome breccias (Jiang et al., 2007; Wang et al., 2016; Li et al., 2017) from base to top. The brecciated dolostone transitions to overlying organic-rich black shale, marking a major facies change similar to that of the Doushantuo Member III/Member IV contact in the Yangtze Gorges area.

The stratigraphic correlation between the JLW and SDP sections is based on litho-, sequence, and chemo-stratigraphic data, which were described in detail by Jiang et al. (2011),

Wang et al. (2016) and Li et al. (2017). The Doushantuo Formation in the JLW and SDP sections as well as in most sections across the Yangtze Platform contains two important stratigraphic markers, i.e., the cap carbonate and the Member IV black shale (Jiang et al., 2011; Zhu et al., 2013; Wang et al., 2016; Li et al., 2017), and comprises three sedimentary cycles. Cycle II at JLW starts with a dark-colored succession at Member □/II, which changes into thickly-bedded dolostone and limestone of Member III (~80-140 m above the boundary of Cap/Nantuo Formation) and into black shale of Member IV (~140-154 m above the boundary of Cap/Nantuo Formation; Cycle III) (McFadden et al., 2008; Jiang et al., 2011). Similar lithofacies changes through Cycles II–III are observed at SDP: from light-grey, thickly-bedded dolostone containing chert layers to shaly/muddy dolostone with banded dark-gray shale (70-115 m), thickly-bedded dolostone and limestone (115-145 m), a partially covered, 10-m-thick (145–155 m) interval of dolostone, a 5-m-thick (155–160 m) brecciated dolostone interval, followed by 6-m-thick (160–166 m) black shales with lenticular limestone and dolostone beds, which transit upwards into bedded cherts and silicified shales of the Liuchapo Formation (Jiang et al., 2011; Wang et al., 2016). In addition, an abrupt facies change that is regarded as a synchronous surface can be identified within the Doushantuo Formation at about 72 m at JLW and 67 m at SDP (Jiang et al., 2011).

Although large variations in $\delta^{13}C_{carb}$ values have been observed in the Doushantuo Formation, at present carbon isotope stratigraphy remains critical to establishing correlations between the Doushantuo Formation and other time-equivalent strata globally. In the Yangtze

Gorges area, the magnitude and timing of the Shuram/DOUNCE event is well expressed across shelf-to-basin transects. Correlation based on $\delta^{13}C$ chemostratigraphy between the JLW and SDP sections was carried out in previous studies (Wang et al., 2016; Li et al., 2017). Both sections show a similar pattern of three prominent negative $\delta^{13}C_{carb}$ excursions (EN1-EN3) separated by two positive intervals (Ediacaran Positive excursion 1-2 or EP1-EP2; at ca. +5 ‰), consistent with $\delta^{13}C_{carb}$ profiles from other locations in the Yangtze Gorges area (Zhou and Xiao, 2007; Li et al., 2017; Wang et al., 2016). The SE shows three distinct intervals of $\delta^{13}C_{carb}$ variation at JLW from base to top: (i) a negative shift from +5 ‰ during EP2 to –9 ‰ over ~20 m (EN3a), (ii) stable values of ca. –9 ‰ over ~33 m (EN3b), and (iii) a positive shift from –9 ‰ to –2 ‰ over >10 m (EN3c) (Fig. 1A). The deeper SDP section shows some differences in detail: (i) a negative shift from +5 ‰ during EP2 to +1.5 ‰ over ~5 m (EN3a), (ii) stable values of ca. +1.5 ‰ over ~60 m (EN3b), and (iii) a pronounced decline to a minimum of –8.3 ‰ followed by a positive shift to +0.1 ‰ (EN3c) (Fig. 1B). Our model of secular variation in seawater sulfate concentrations during the SE is based on this subdivision. However, in view of the large increases of $\delta^{34}S_{CAS}$ and [CAS] in the upper part of EN3b at JLW, we further subdivided EN3b into EN3b-1 and EN3b-2 in order to track high-frequency changes in the marine sulfur cycle. Similarly, we subdivided EN3c into EN3c-1 and EN3c-2 in order to distinguish pronounced increases and decreases of $\delta^{34}S_{CAS}$ and [CAS] at SDP during this interval (Fig. 1).

Analytical Methods

A total of 154 new samples were collected and analyzed from the JLW (57) and SDP (97) sections in this study, yielding paired $\delta^{34}S_{CAS}$-$\delta^{34}S_{py}$ and [CAS] data. Samples were collected at intervals of 0.3 to 4 m throughout each section, with care taken to avoid shale beds. Weathered surfaces and obvious diagenetic phases were trimmed off prior to powdering. In the laboratory, samples were first crushed into granules, and then the freshest pieces were chosen and crushed to finer than 200 mesh using a Retsch RS 200 vibratory disc mill. Geochemical results are summarized in Tables DR1 and DR4.

Carbonate-associated sulfate (CAS) sulfur isotopes. CAS was extracted using the method of Burdett et al. (1989) as modified by Luo et al. (2010). For each sample with TIC >3 %, ~20-50 g of powder was washed in a 10 % NaCl solution for 24 h, and after gravitational settling, the supernatant was aspirated and the residual powder was rinsed with 18.25 MΩ distilled water. These steps were repeated until no barite precipitate formed when saturated $BaCl_2$ solution (~250 g/L) was added to the supernatant (i.e., all sulfate was removed). The residual powder was then dissolved through slow addition of 4 M HCl and stirring until the reaction went to completion. About 125 mL of a saturated $BaCl_2$ solution was then added in order to precipitate dissolved sulfate as barium sulfate ($BaSO_4$), which was dried and weighed for calculation of the CAS concentration (ppm) in the carbonate fraction of each sample after correction for the amount of insoluble material (assuming that all of the dissolved material was pure carbonate). The isotopic composition of dried $BaSO_4$ (representing recovered CAS, thus $\delta^{34}S_{CAS}$) was measured on a Thermo Fisher Scientific

Delta V Plus isotope ratio mass spectrometer coupled with a Flash elemental analyzer in the State Key Laboratory of Biogeology and Environmental Geology, China University of Geosciences-Wuhan (CUG-W). Results are expressed in standard delta notation as per mille deviations relative to the international Vienna Cañon Diablo Troilite (VCDT) standard, where $\delta^{34}S = [(^{34}S/^{32}S)_{sample} / (^{34}S/^{32}S)_{standard} - 1] \times 1000$ ‰. Analytical reproducibility was generally better than ±0.2 ‰ (1σ) calculated from replicate analyses of IAEA standards [NBS-127 (21.1‰), IAEA-SO-5 (0.49‰), IAEA-SO-6 (-34.05‰)].

Pyrite extraction and sulfur isotopes. Pyrite sulfur in whole-rock samples was extracted using the chromium reduction method (Canfield et al., 1986). Pyrite extractions were carried out in 20 ml concentrated HCl and 40 ml 1 M chromous chloride solutions for 2 h while heated under an N_2 atmosphere. The pyrite sulfur was collected as silver sulfide, which was dried and weighed to determine pyrite sulfur concentrations. The resulting Ag_2S was combined with an excess of V_2O_5 and combusted online for measurement of pyrite sulfur isotopic compositions ($\delta^{34}S_{py}$) on a Thermo Fisher Scientific Delta V Plus isotope ratio mass spectrometer (IRMS) coupled with a Flash elemental analyzer at the State Key Laboratory of Biogeology and Environmental Geology (CUG-W). Results are expressed in standard delta notation as per mille deviations relative to VCDT with an analytical error better than ±0.2 ‰ (1σ) calculated from replicate analyses of IAEA standards [IAEA-S1 (-0.3‰), IAEA-S2 (22.65‰), IAEA-S3 (-32.5‰)].

Elemental concentrations. About 50 mg of dried whole-rock sample powder was dissolved using a standard HNO_3-HF digestion as described below. The digestion step

204 included progressive acid treatments at 190 °C in a 15-ml Teflon bomb equipped with a
205 screw cap to which HNO_3-HF (1:1) and HNO_3 were sequentially added until complete
206 digestion was achieved. Distilled HNO_3 and trace-metal-grade HF reagents were used for all
207 samples. Following an evaporation procedure to remove concentrated acid, the sample was
208 diluted with 2 % nitric acid, which was followed by analysis using either an Agilent 7700x
209 inductively coupled plasma mass spectrometer (ICP-MS) for rare earth elements (REEs) or a
210 Thermo Fisher ICAP 7400 inductively coupled plasma optical emission spectrometry
211 (ICP-OES) for Fe, Ca, and Mg concentrations. Analytical errors are better than ±2.1 % for
212 Fe, ±1 % for Ca, and ±0.6 % for Mg based on analyses of USGS (BCR-2, AGV-2, BHVO-2,
213 RGM-2) and Chinese (GSR5) standards.

214 **Pyrite framboid size measurements.** Fifteen samples from JLW (7) and SDP (8) were
215 selected for analysis of pyrite framboid size distributions. Two or three polished blocks of
216 each sample (2 cm × 2 cm) were made for *in situ* observation and measurement of pyrite
217 framboids with a FEI Quanta 200 scanning electron microscope (SEM) at the State Key
218 Laboratory of Geological Processes and Mineral Resources (CUG-W). The spatial
219 resolution of the secondary electron image of SEM is better than 3.5 μm. In backscattered
220 electron (BSE) images, framboidal and euhedral pyrite crystals are easily distinguished by
221 their shape and structure (Fig. DR7). The diameters of framboidal and euhedral pyrite
222 crystals were measured directly on the SEM screen, with a precision of better than 0.1 μm.
223

224 **Seawater Sulfate Concentration Model and Age Sensitivity Analysis**

Rate method of seawater sulfate concentration estimation

Paleo-seawater sulfate concentrations ($[SO_4^{2-}]_{sw}$) were estimated using the "rate method" of Algeo et al. (2015), as modified from Kurtz et al. (2003) and Kah et al. (2004). In this method, $[SO_4^{2-}]_{sw}$ is constrained based on two input parameters: (1) the difference in S-isotopic compositions between cogenetic sedimentary sulfate and sulfide ($\Delta^{34}S_{CAS-py}$), and (2) the observed maximum rate of change in seawater sulfate $\delta^{34}S$, i.e., $\partial\delta^{34}S_{CAS}/\partial t(max)$. These two parameters are related to each other as a function of the mass of seawater sulfate (M_o) and the burial flux of reduced (mainly pyrite) sulfur (F_{py}) [see Algeo et al. (2015), for equations and derivations]. $[SO_4^{2-}]_{sw}$ is estimated from the relationship as follows:

$$\partial\delta^{34}S_{CAS}/\partial t = [F_{in} \times (\delta^{34}S_{in} - \delta^{34}S_{sw}) - F_{py} \times \Delta^{34}S] / M_o \quad (1)$$

$$[SO_4^{2-}]_{sw} = k_1 \times k_2 \times M_o \quad (2)$$

F_{in} is the total input flux of sulfur to the ocean system from weathering, which is allowed to vary. $\delta^{34}S_{in}$ represents the isotopic composition of fluxes associated with weathering and sulfate deposition, M_o is the mass of sulfate sulfur in the oceans (calculated), and $\Delta^{34}S$ is the observed fractionation between oxidized and reduced sulfur reservoirs ($\Delta^{34}S = \delta^{34}S_{CAS} - \delta^{34}S_{py}$). The terms k_1 (= 10^6) and k_2 (= 2.22×10^{-20} mM g^{-1}) are conversion constants. Because of a paucity of evaporites in the Precambrian and the small S-isotopic fractionation associated with their deposition, we disregard the evaporite burial sink flux (i.e., $F_{evaporite}$ and $\delta^{34}S_{evaporite}$) in our calculations.

Secular variation in seawater sulfate $\delta^{34}S$ is thought to be due mainly to changes in the proportions of the sink fluxes, with increasing (decreasing) burial of pyrite relative to sulfate

246 leading to more (less) ^{34}S-enriched $\delta^{34}S_{sw}$ (Bottrell and Newton, 2006; Halevy et al., 2012).
247 We varied $\Delta^{34}S_{CAS\text{-}py}$ from 1 to 100 ‰ for five discrete log-interval values of
248 $\partial\delta^{34}S_{CAS}/\partial t(max)$ ranging from 1 to 100 ‰ Myr^{-1} (Fig. DR2). From Equation 1, the
249 maximum rate of isotope change is reached when S inputs to the ocean approach zero (F_{in} =
250 0) and the standing seawater sulfate reservoir is removed as pyrite ($F_{py} = F_{in}$), giving:

251 $$\partial\delta^{34}S_{CAS}/\partial t(max) = k_1 \times F_{py} \times \Delta^{34}S / M_o \quad (3)$$

252 Because observed values of $\partial\delta^{34}S_{CAS}/\partial t(max)$ are generally smaller than the theoretical
253 maximum rate, the resulting estimates of $[SO_4^{2-}]_{sw}$ are generally larger than actual seawater
254 sulfate concentrations during the interval of interest. Thus, $[SO_4^{2-}]_{sw}$ estimates based on
255 $\partial\delta^{34}S_{CAS}/\partial t(max)$ commonly represent *maximum* possible seawater sulfate concentrations for
256 a given interval.

257 High maximum rates of change (i.e., large $\partial\delta^{34}S_{CAS}/\partial t(max)$) are associated with a
258 small seawater sulfate reservoir, because $\partial\delta^{34}S_{CAS}$ is not well-buffered in a low-$[SO_4^{2-}]_{sw}$
259 system. In contrast, low maximum rates of changes (i.e., $\partial\delta^{34}S_{CAS}/\partial t \leq 0.7$ ‰ Myr^{-1}) are
260 observed since 65 Ma (Paytan et al., 1998) because of the high $[SO_4^{2-}]_{sw}$ of Cenozoic oceans
261 (e.g., 29 mM for the modern; Millero, 2005). Owing to lower atmospheric pO_2 and evaporite
262 weathering rates than in the modern, F_{py} was lower for Neoproterozoic oceans. Thus, a value
263 of 10×10^{13} g yr^{-1} is appropriate for the burial flux of sulfur in anoxic ancient oceans, in
264 which pyrite sulfur is the dominant sink flux for seawater sulfate assuming a steady-state
265 condition for the marine sulfur cycle (Song et al., 2014; Luo et al., 2015; Algeo et al., 2015).

Calculation of $\partial\delta^{34}S_{CAS}/\partial t(max)$ for a sedimentary unit of interest requires information regarding sedimentation rates, which can be highly uncertain for Proterozoic successions. One approach is to assume a range of typical sedimentation rates (e.g., Kah et al., 2004). Instead, we used recently published geochronological data in Condon et al. (2005), Zhang et al. (2005), Kendall et al. (2015), and Wang et al. (2016) for the onset of the Doushantuo SE (see sections above) to constrain sedimentation rates for each study unit based on its thickness and maximum possible duration. Our sedimentation rate estimates for the SE of the Doushantuo Formation are 4.0 m Myr^{-1} for EP2-EN3b and 1.6 m Myr^{-1} for EN3c at JLW, and 4.7 m Myr^{-1} for EP2-EN3b and 2.5 m Myr^{-1} for EN3c at SDP. For each unit, $\partial\delta^{34}S_{CAS}/\partial t(max)$ was calculated based on the largest measured isotopic shift defined by a minimum of three consecutive data points and the range of sedimentation rate estimates (i.e., average and maximum) as given in Table DR3.

Age sensitivity analysis

Our sulfate concentration model depends on the change rate of seawater sulfate isotope ($\partial\delta^{34}S_{CAS}/\partial t$). Although our age model for the Doushantuo Formation is reasonably robust (see **Geological Setting**), there are uncertainties in two of the age-point anchors (i.e., at 575 and 560 Ma). Here, we consider a range of possible age errors and their potential influences on calculated rates in our model, and we undertake a simple sensitivity analyses to explore the parameter space of sediment accumulation rate.

Six age errors of −1, +1, −5, +5, −10, and +10 (Myr) are assumed for the 575 and 560 Ma age-point anchors to evaluate the sensitivity of calculated accumulation rates and modeled seawater sulfate concentrations. First, we modified just the 575 Ma age-point anchor by 1, 5, or 10 Myr, keeping all other age parameters constant. The results show that a ±1-Myr adjustment resulted in little change in accumulation rates and sulfate concentrations (Table DR5), a ±5-Myr adjustment resulted in moderate changes in accumulation rates and sulfate concentrations (Fig. 2; Table DR5), and a ±10-Myr adjustment resulted in large changes in accumulation rates and sulfate concentrations (Table DR5). However, we note that, although all age adjustments modify the absolute values of modeled $[SO_4^{2-}]_{sw}$, they do not affect secular trends in $[SO_4^{2-}]_{sw}$ or differences in $[SO_4^{2-}]_{sw}$ between the two study sections. For this reason, they do not impact our conclusions regarding a transient increase in seawater sulfate concentrations during the SE and a lateral sulfate gradient across the Yangtze Platform.

Modeling results of marine sulfate concentrations in Oman

Model estimates of marine sulfate concentrations in the Ediacaran Shuram Formation of Oman (Fig. DR3; basic data are from Fike et al., 2006) share many features with the Doushantuo Shuram/DOUNCE event discussed in the main text. Due to limited dating data, model calculations are only divided into two intervals, i.e., before and after ~580 Ma (Gaskiers Glaciation), showing an increase in $[SO_4^{2-}]_{sw}$ from <2 mM (Loyd et al., 2012; Osburn et al., 2015) to ~8 mM (mean in which the pyrite burial flux is equal to 10×10^{13} g

307 yr^{-1} in an anoxic ocean). These data are generally consistent with a progressive oxidation of
308 the SE ocean after the Gaskiers Glaciation. Although it is difficult to gauge absolute
309 Ediacaran marine sulfate concentrations, our estimates for South China and Oman suggest
310 that $[SO_4^{2-}]_{sw}$ increased after the Gaskiers Glaciation but did not exceed ~10 mM in the shelf
311 areas, which is appreciably lower than the modern value of 28.4 mM.

312 Given uncertainties in stratigraphic ages and sedimentation rates, the model estimates for
313 the Oman Shuram $[SO_4^{2-}]_{sw}$ can serve only as a rough guide. Firstly, the average deposition
314 rate of the Shuram Formation in Oman is estimated to have been ~18 m Myr^{-1}, which is
315 somewhat over rapid for "rate method" modeling (ref. Kah et al., 2004, Loyd et al., 2012).
316 Secondly, there is no detailed age framework for subdivision of the Oman Shuram
317 Formation, thus impeding an evaluation of the segmented evolution of $[SO_4^{2-}]_{sw}$, as for JLW
318 and SDP in South China. The Shuram Excursion in Oman is limited only by two age
319 constraints: ~580 Ma (Sawaki et al., 2010), and ~550 Ma for the mid-Buah (correlation with
320 Doushantuo Formation, China; Bowring et al., 2007; Condon et al., 2005). A detailed
321 analysis of the Shuram Excursion in Oman is not possible owing to a lack of age constraints
322 for the $\delta^{13}C_{carb}$ minimum (Fike et al., 2006) and an unconformity across the Khufai–Shuram
323 boundary that probably includes the interval of the Gaskiers Glaciation.

324

325 **Evaluation of Sulfate Residence Times in the Ediacaran Ocean**

326 In modern oceans, sulfate concentrations are uniformly ~29 mM with a source flux of
327 1.5×10^{18} mol Myr^{-1} (Kump and Garrels, 1986), and no lateral or vertical seawater gradients

exist. This condition reflects the fact that the seawater sulfate residence time (~13 Myr) is far longer than the oceanic mixing time of ~1-2 kyr. In order for a lateral sulfate gradient to exist, as observed in the present study of the Ediacaran Yangtze Platform, it requires the seawater sulfate residence time to be comparable to or shorter than the contemporaneous oceanic mixing time. Although the Ediacaran oceanic mixing time is unknown, it could theoretically be much longer than that of the modern ocean (~1-2 kyr) given widespread oceanic redox stratification and spatial heterogeneity (see review in Bowyer et al., 2017).

The residence time of Ediacaran seawater sulfate can be quantitatively estimated based on $[SO_4^{2-}]_{sw}$ and riverine sulfate fluxes. We estimated the residence time (τ) of seawater sulfate during the SE interval by using a simple linear response system model (Henderson, 1982) (Fig. DR4). In the box for the seawater sulfate reservoir, change of reservoir mass per unit time (dM/dt) is controlled by differences between riverine source (F_{in}) and sediment sink (F_{out}) fluxes, which are expressed as:

$$\frac{dM}{dt} = F_{in} - F_{out} \quad (4)$$

where the F_{out} is proportional to M,

$$F_{out} = KM \quad (5)$$

and K is a rate constant. Then:

$$\frac{dM}{dt} = F_{in} - KM \quad (6)$$

Assuming the seawater sulfate reservoir is in a steady-state condition on a long (i.e., multi-million-year) timescale, then $\frac{dM}{dt} = 0$, and

$$\frac{1}{K} = \tau = \frac{M}{F_{in}} \quad (7)$$

In this case, the residence time (τ) shows a negative correlation with sulfate source fluxes (F_{in}) and a positive correlation with oceanic sulfate reservoir, as shown in Figure DR5. Thus, seawater sulfate residence times decline with decreasing marine sulfate reservoir mass and increasing sulfate weathering fluxes. Our modeling results indicate that if the Ediacaran oceanic sulfate reservoir were low to e.g., ~0.3 mM or ~0.1 mM, then a seawater sulfate residence time of ~2000 years would require a riverine sulfate flux only ~60× to ~20× the present flux (see red lines in Fig. DR5; Table DR6).

These conditions may have been met on the Yangtze Platform during the SE. Earlier studies have inferred $[SO_4^{2-}]_{sw}$ of <2 mM for shallow carbonate platforms and lower for distal shelves before the SE (e.g., Loyd et al., 2012; Osburn et al., 2015), and our $[SO_4^{2-}]_{sw}$ estimates for the SE is <~3 mM in distal areas beyond the upper-slope SDP (Fig. 2) during the SE; all of these values are consistent with average Ediacaran $[SO_4^{2-}]_{sw}$ having been extremely low. Furthermore, the sulfate concentrations of modern fluvial systems are ~1.5-7500 μM for streams and ~22-600 μM for rivers, indicating a large variation of riverine sulfate fluxes (over 3 orders of magnitude) (Meybeck and Helmer, 1989; Chen et al., 2002). As indicated by transient increases of our modeled $[SO_4^{2-}]_{sw}$, riverine sulfate weathering fluxes may have been greatly elevated during the SE. Elevated sulfate weathering fluxes are consistent with increases in marine carbonate $^{87}Sr/^{86}Sr$ ratios from <0.708 to >0.709 in South China (Sawaki et al., 2010) and globally (see figure 5 of Li et al., 2017), probably as a consequence of the ~600-550 Ma Pan-African orogeny (Ross et al., 1995; Canfield, 2004). Although accurate constraints on Edacaran $[SO_4^{2-}]_{sw}$ and sulfate weathering fluxes are

absent, the considerations above support a much shorter residence time of seawater sulfate and potentially longer oceanic mixing time for Ediacaran oceans. Thus, a lateral sulfate gradient potentially could have developed across continental shelves such as the Yangtze Platform during the Ediacaran.

Data Evaluation

Diagenetic influences on primary marine carbonate signals (e.g., $\delta^{13}C_{carb}$) at study sections have been carefully evaluated in Li et al. (2017) by using combined stratigraphic, petrographic, mineralogical, and geochemical (e.g., Mn/Sr, $\delta^{18}O_{carb}$ and cross plot of $\delta^{13}C_{carb}$ versus $\delta^{18}O_{carb}$) data, which indicate no to very imited burial diagenesis and thus primary marine carbonate signature preserved for the SE at study sections. In addition, previous study indicated that even intense meteoric diagenesis has very little effects on $\delta^{34}S_{CAS}$ (Gill et al., 2008). We therefore conclude that our $\delta^{34}S_{CAS}$ signatures are primary and that the [CAS] was not significantly modified although it is vulnerable to diagenetic resetting (Gill et al., 2008).

Pyrite and organic S are generally strongly ^{34}S-depleted relative to co-occurring sulfate (Zaback and Pratt, 1992), and oxidation of pyrite during CAS extraction can significantly lower measured $\delta^{34}S_{CAS}$ values (Marenco et al., 2008a). However, [CAS] does not show significant covariation with either total Fe (R^2 = 0.10 at JLW and 0.09 at SDP; Fig. DR6B) or pyrite S (R^2 = 0.14 at JLW and 0.003 at SDP; Fig. DR6D). Furthermore, $\delta^{34}S_{CAS}$ exhibits no covariation with either total Fe or pyrite S (R^2 = 0.10 at JLW and 0.06 at SDP, and R^2 =

391 0.12 at JLW and 0.14 at SDP, respectively; Fig. DR6A, C). Collectively, these covariant
392 relationships indicate that [CAS] and $\delta^{34}S_{CAS}$ were not measurably influenced by oxidation
393 of the pyrite or organic sulfur fractions of the sediment.

394 Ca/Mg ratios provide a measure of the degree of dolomitization of carbonate sediment,
395 a process that can influence the sulfur isotopic composition of CAS (Marenco et al., 2008b).
396 In the study sections, Ca/Mg ratios are mostly < 2 in EP2 to EN3b-1 but >20 in EN3b-2 (Fig.
397 DR6E-F), which accords with the lithologic descriptions given in above sections. However,
398 neither [CAS] nor $\delta^{34}S_{CAS}$ covaries significantly with Ca/Mg ratio (both $R^2 \leq 0.20$; Fig.
399 DR6E-F). We therefore infer that there is no evidence for the influence of dolomitization on
400 our $\delta^{34}S_{CAS}$ data.

401

402 **Pyrite Framboid Size Distributions and Their Implications for Water-Column**
403 **Formation of Pyrites**

404 Modern marine systems provide a guide for assessing whether pyrite crystals are
405 syngenetic or diagenetic in origin based on their shapes and diameters (Wilkin and Barnes,
406 1996). Using scanning electron microscope (SEM) analysis, pyrite was found throughout the
407 study section in the form of both framboids and euhedral crystals. As a common authigenic
408 mineral, pyrite occurs as euhedral crystals or framboids in ancient anoxic facies. In euxinic
409 water columns, pyrite forms near the chemocline and then sinks to the sediment-water
410 interface. Owing to a critical threshold size for rapid sinking of framboids, they tend to
411 exhibit relatively uniform and small sizes (generally < 10 μm) in the sediment. Beneath oxic

412 water columns, pyrite forms mainly in the sulfidic zone of the sediment column. Because of
413 variation in the time-integrated availability of Fe and H_2S in the porewater environment, any
414 pyrite framboids formed there tend to show larger size (commonly with individual
415 framboids exceeding 10 μm in diameter) and considerable size variation, and framboidal
416 clusters and euhedral pyrite crystals can also form. In some cases, syngenetically formed
417 framboids acquire diagenetic overgrowths in the burial environment (Wilkin and Barnes,
418 1996).

419 Micron-scale pyrite crystals are found randomly distributed and in isolation in studied
420 samples of the SE interval. Three types of pyrite were identified during BSE investigation of
421 our samples: (1) small framboids (< 10 μm, closely packed, spherical aggregates of
422 uniform-sized microcrystals) of probable syngenetic origin (Fig. DR7A, B, F-H); (2)
423 medium-size (10-14 μm) subhedral pyrite framboids, representing diagenetic overgrowths
424 on syngenetic framboids (Fig. DR7C-D); and (3) large (>10 μm) euhedral pyrite crystals of
425 diagenetic origin (Fig. DR7E). Where present, we measured >50 framboids in each sample.
426 A large majority of the framboids (>93 %) are <10 μm in diameter (Fig. DR8) and likely
427 formed in the water column (Wilkin and Barnes, 1996). The mean sizes of framboids vary to
428 only a limited degree between samples, clustering around 7-9 μm, with standard deviations
429 mostly <2 μm, which is consistent with a predominantly syngenetic origin (Fig. DR8).
430 Sporadic larger framboids (>10 μm) may represent diagenetic precipitates or overgrowths on
431 earlier-formed syngenetic framboids, as suggested by visible overgrowths on some
432 individual crystals (Fig. DR7D-E).

References

Ader, M., Macouin, M., Trindade, R.I.F., Hadrien, M., Yang, Z., Sun, Z., and Besse, J., 2009, A multilayered water column in the Ediacaran Yangtze Platform? Insights from carbonate and organic matter paired $\delta^{13}C$: Earth and Planetary Science Letters, v. 288, p. 213-227.

Algeo, T.J., Luo, G.M., Song, H.Y., Lyons, T.W., and Canfield, D.E., 2015, Reconstruction of secular variation in seawater sulfate concentrations: Biogeosciences, v. 12, p. 2131-2151.

An, Z., Jiang, G., Tong, J., Tian, L., Ye, Q., Song, H.Y., and Song, H.J., 2015, Stratigraphic position of the Ediacaran Miaohe biota and its constrains on the age of the upper Doushantuo $\delta^{13}C$ anomaly in the Yangtze Gorges area, South China: Precambrian Research, v. 271, p. 243-253.

Bottrell, S.H., and Newton, R.J., 2006, Reconstruction of changes in global sulfur cycling from marine sulfate isotopes: Earth-Science Reviews, v. 75, p. 59-83.

Bowring, S.A., Grotzinger, J.P., Condon, D.J., Ramezani, J., Newall, M.J., and Allen, P.A., 2007, Geochronologic constraints on the chronostratigraphic framework of the Neoproterozoic Huqf Supergroup, Sultanate of Oman: American Journal of Science, v. 307, p. 1097-1145.

Bowyer, F., Wood, R.A., and Poulton, S.W., 2017, Controls on the evolution of Ediacaran metazoan ecosystems: A redox perspective: Geobiology, v. 15, p. 516-551.

Burdett, J.W., Arthur, M.A. and Richardson, M.A., 1989, Neogene seawater sulfur isotope age curve from calcareous pelagic microfossils: Earth and Planetary Science Letters, v. 94, p. 189-198.

Calver, C.R., 2000, Isotope stratigraphy of the Ediacarian (Neoproterozoic III) of the Adelaide Rift Complex, Australia, and the overprint of water column stratification: Precambrian Research, v. 100, p. 121-150.

Canfield, D.E., 2004, The evolution of the Earth surface sulfur reservoir: American Journal of Science, v. 304, p. 839-861.

Canfield, D.E., Raiswell, R., Westrich, J.T., Reaves, C.M., and Berner, R.A., 1986, The use of chromium reduction in the analysis of reduced inorganic sulfur in sediments and shales: Chemical Geology, v. 54, p. 149-155.

Chen, D.F., Dong, W.Q., Zhu, B.Q., and Chen, X.P., 2004, Pb–Pb ages of Neoproterozoic Doushantuo phosphorites in South China: constraints on early metazoan evolution and glaciation events: Precambrian Research, v. 132, p. 123-132.

Chen, J., Wang, F., Xia, X., and Zhang, L., 2002, Major element chemistry of the Changjiang (Yangtze River): Chemical Geology, v. 187, p. 231-255.

Chen, Z., Zhou, C., Xiao, S., Wang, W., Guan, C., Hua, H., and Yuan, X., 2014, New Ediacara fossils preserved in marine limestone and their ecological implications: Scientific Reports, v. 4, p. 4180.

Condon, D., Zhu, M., Bowring, W., Wang, W., Yang, A., and Jin, Y., 2005, U-Pb Ages from the Neoproterozoic Doushantuo Formation, China: Science, v. 308, p. 95-98.

Ding, L., Li, Y., Hu, X., Xiao, Y., Su, C., and Huang, J., 1996, Sinian Miaohe Biota: Beijing, Geological Publishing House, 221 pp.

Droser, M.L., and Gehling, J.G., 2015, The advent of animals: The view from the Ediacaran: Proceedings of the National Academy of Sciences (U.S.A.), v. 112, p. 4865-4870.

Fike, D.A., Grotzinger, J.P., Pratt, L.M., and Summons, R.E., 2006, Oxidation of the Ediacaran ocean: Nature, v. 444, p. 744-747.

Gill, B.C., Lyons, T.W., and Frank, T.D., 2008, Behavior of carbonate-associated sulfate during meteoric diagenesis and implications for the sulfur isotope paleoproxy: Geochimica et Cosmochimica Acta, v. 72, p. 4699-4711.

Halevy, I., Peters, S.E., and Fischer, W.W., 2012, Sulfate burial constraints on the Phanerozoic sulfur cycle: Science, v. 337, p. 331-334.

Halverson, G.P., Hoffman, P.F., Schrag, D.P., Maloof, A.C., and Rice, A.H.N., 2005, Toward a Neoproterozoic composite carbon-isotope record: Geological Society of America Bulletin, v. 117, p. 1181-1207.

Henderson, P., 1982, Inorganic Geochemistry, Pergamon, Oxford, 367 pp.

Jiang, G., Christie-Blick, N., Kaufman, A.J., Banerjee, D.M., and Rai, V., 2002, Sequence stratigraphy of the Neoproterozoic Infra Krol Formation and Krol Group, Lesser Himalaya, India: Journal of Sedimentary Research, v. 72, p. 524-542.

Jiang, G., Kennedy, M.J., and Christie-Blick, N., 2003, Stable isotopic evidence for methane seeps in Neoproterozoic postglacial cap carbonates: Nature, v. 426, p. 822-826.

Jiang, G., Kennedy, M.J., Christie-Blick, N., Wu, H., and Zhang, S., 2006, Stratigraphy, sedimentary structures, and textures of the late Neoproterozoic Doushantuo cap carbonate in South China: Journal of Sedimentary Research, v. 76, p. 978-995.

Jiang, G., Kaufman, A.J., Christie-Blick, N., Zhang, S., and Wu, H., 2007, Carbon isotope variability across the Ediacaran Yangtze platform in South China: Implications for a large surface-to-deep ocean $\delta^{13}C$ gradient: Earth and Planetary Science Letters, v. 261, p. 303-320.

Jiang, G., Wang, X., Shi, X., Zhang, S., Xiao, S., and Dong, J., 2010, Organic carbon isotope constraints on the dissolved organic carbon (DOC) reservoir at the Cryogenian-Ediacaran transition: Earth and Planetary Science Letters, v. 299, p. 159-168.

Jiang, G., Shi, X., Zhang, S., Wang, Y., and Xiao, S., 2011, Stratigraphy and paleogeography of the Ediacaran Doushantuo Formation (ca. 635-551 Ma) in South China: Gondwana Research, v. 19, p. 831-849.

Kah, L.C., Lyons, T.W., and Frank, T.D., 2004, Low marine sulphate and protracted oxygenation of the Proterozoic biosphere: Nature, v. 431, p. 834-838.

Kaufman, A.J., Jiang, G., Christie-Blick, N., Banerjee, D.M., and Rai, V., 2006, Stable isotope record of the Neoproterozoic Krol Platform in the Lesser Himalaya of northern India: Precambrian Research, v. 147, p. 156-185.

Kaufman, A.J., Corsetti, F.A., and Varni, M.A., 2007, The effect of rising atmospheric oxygen on carbon and sulfur isotope anomalies in the Neoproterozoic Johnnie Formation, Death Valley, USA: Chemical Geology, v. 237, p. 47-63.

Kendall, B., Komiya, T., Lyons, T.W., Bates, S.M., Gordon, G.W., Romaniello, S.J., Jiang, G., Creaser, R.A., Xiao, S., McFadden, K., Sawaki, Y., Tahata, M., Shu, D., Han, J., Li, Y., Chu, X., and Anbar, A.D., 2015, Uranium and molybdenum isotope evidence for an episode of widespread ocean oxygenation during the late Ediacaran Period: Geochimica et Cosmochimica Acta, v. 156, p. 173-193.

Kurtz, A.C., Kump, L.R., Arthur, M.A., Zachos, J.C., and Paytan, A., 2003, Early Cenozoic decoupling of the global carbon and sulfur cycles: Paleoceanography, v. 18. pp.

Kump, L.R., Garrels, R.M., 1986, Modeling atmospheric O_2 in the global sedimentary redox cycle: American Journal of Science, v. 286, p. 337-370.

517 Le Guerroué, E., and Cozzi, A., 2010, Veracity of Neoproterozoic negative C-isotope values: The
518 termination of the Shuram negative excursion: Gondwana Research, v. 17, p. 653-661.
519 Le Guerroué, E., Allen, P.A., Cozzi, A., Etienne, J.L., and Fanning, M., 2006, 50 Myr recovery from the
520 largest negative $\delta^{13}C$ excursion in the Ediacaran ocean: Terra Nova, v. 18, p. 147-153.
521 Li, C., Love, G.D., Lyons, T.W., Fike, D.A., Sessions, A.L., and Chu, X., 2010, A stratified redox model
522 for the Ediacaran ocean: Science, v. 328, p. 80-83.
523 Li, C., Hardisty, D.S., Luo, G., Huang, J., Algeo, T.J., Cheng, M., Shi, W., An, Z., Tong, J., Xie, S., Jiao,
524 N., and Lyons, T.W., 2017, Uncovering the spatial heterogeneity of Ediacaran carbon cycling:
525 Geobiology, v. 15, p. 211-224.
526 Li, C., Planavsky, N.J., Shi, W., Zhang, Z., Zhou, C., Cheng, M., Tarhan, L.G., Luo, G., and Xie, S., 2015,
527 Ediacaran Marine Redox Heterogeneity and Early Animal Ecosystems: Scientific Reports, v. 5, p.
528 17097.
529 Liu, P., Yin, C., Chen, S., Tang, F., and Gao, L., 2013, The biostratigraphic succession of acanthomorphic
530 acritarchs of the Ediacaran Doushantuo Formation in the Yangtze Gorges area, South China and its
531 biostratigraphic correlation with Australia: Precambrian Research, v. 225, p. 29-43.
532 Loyd, S.J., Marenco, P.J., Hagadorn, J.W., Lyons, T.W., Kaufman, A.J., Sour-Tovar, F., and Corsetti,
533 F.A., 2012, Sustained low marine sulfate concentrations from the Neoproterozoic to the Cambrian:
534 Insights from carbonates of northwestern Mexico and eastern California: Earth and Planetary
535 Science Letters, v. 339-340, p. 79-94.
536 Lu, M., Zhu, M., Zhang, J., Shields-Zhou, G., Li, G., Zhao, F., Zhao, X., and Zhao, M., 2013, The
537 DOUNCE event at the top of the Ediacaran Doushantuo Formation, South China: Broad
538 stratigraphic occurrence and non-diagenetic origin: Precambrian Research, v. 225, p. 86-109.
539 Luo, G., Kump, L.R., Wang, Y., Tong, J., Arthur, M.A., Yang, H., Huang, J., Yin, H., and Xie, S., 2010,
540 Isotopic evidence for an anomalously low oceanic sulfate concentration following end-Permian mass
541 extinction: Earth and Planetary Science Letters, v. 300, p. 101-111.
542 Luo, G., Ono, S., Huang, J., Algeo, T.J., Li, C., Zhou, L., Robinson, A., Lyons, T.W., and Xie, S., 2015,
543 Decline in oceanic sulfate levels during the early Mesoproterozoic: Precambrian Research, v. 258, p.
544 36-47.
545 Marenco, P.J., Corsetti, F.A., Kaufman, A.J. and Bottjer, D.J., 2008a, Environmental and diagenetic
546 variations in carbonate associated sulfate: an investigation of CAS in the Lower Triassic of the
547 western USA: Geochimica et Cosmochimica Acta, v. 72, p. 1570-1582.
548 Marenco, P.J., Corsetti, F.A., Hammond, D.E., Kaufman, A.J., and Bottjer D. J., 2008b, Oxidation of
549 pyrite during extraction of carbonate associated sulfate: Chemical Geology, v. 247, p. 124-132.
550 McFadden, K.A., Huang, J., Chu, X., Jiang, G., Kaufman, A.J., Zhou, C., Yuan, X., and Xiao, S., 2008,
551 Pulsed oxidation and biological evolution in the Ediacaran Doushantuo Formation: Proceedings of
552 the National Academy of Sciences (U.S.A), v. 105, p. 3197-3202.
553 McFadden K A, Xiao S, Zhou C, et al. 2009. Quantitative Evaluation of the Biostratigraphic Distribution
554 of Acanthomorphic Acritarchs in the Ediacaran Doushantuo Formation in the Yangtze Gorges Area,
555 South China. Precambrian Research, 173: 170-190.
556 Meybeck, M., and Helmer, R., 1989, The quality of rivers: from pristine stage to global pollution:
557 Palaeogeography, Palaeoclimatology, Palaeoecology, v. 75, p. 283-309.
558 Millero, F.J., 2005, Chemical Oceanography, 3rd ed., CRC Press, Boca Raton, Florida, 536 pp.

559 Narbonne, G.M., 2005, The Ediacaran biota: Neoproterozoic origin of animals and their ecosystems:
560 Annual Review of Earth and Planetary Sciences, v. 33, p. 421-442.
561 Osburn, M.R., Owens, J., Bergmann, K.D., Lyons, T.W., and Grotzinger, J.P., 2015, Dynamic changes in
562 sulfate sulfur isotopes preceding the Ediacaran Shuram Excursion: Geochimica et Cosmochimica
563 Acta, v. 170, p. 204-224.
564 Paytan, A., Kastner, M., Campbell, D., and Thiemens, M.H., 1998, Sulfur isotopic composition of
565 Cenozoic seawater sulfate: Science, v. 282, p. 1459-1462.
566 Ross, G.M., Bloch, J.D., and Krouse, H.R., 1995, Neoproterozoic strata of the southern Canadian
567 Cordillera and the isotopic evolution of seawater sulfate: Precambrian Research, v. 73, p. 71-99.
568 Sahoo, S.K., Planavsky, N.J., Jiang, G., Kendall, B., Owens, J.D., Wang, X., Shi, X., Anbar, A.D., and
569 Lyons, T.W., 2016, Oceanic oxygenation events in the anoxic Ediacaran ocean: Geobiology, v. 14,
570 p. 457-468.
571 Sawaki, Y., Ohno, T., Tahata, M., Komiya, T., Hirata, T., Maruyama, S., Windley, B.F., Han, J., Shu, D.,
572 and Li, Y., 2010, The Ediacaran radiogenic Sr isotope excursion in the Doushantuo Formation in
573 the Three Gorges area, South China: Precambrian Research, v. 176, p. 46-64.
574 Saylor, B.Z., Kaufman, A.J., Grotzinger, J.P., and Urban, F., 1998, A composite reference section for
575 terminal Proterozoic strata of southern Namibia: Journal of Sedimentary Research, v. 68, p.
576 1223-1235.
577 Song, H.Y., Tong, J., Algeo, T.J., Song, H.J., Qiu, H., Zhu, Y., Tian, L., Bates, S., Lyons, T.W., Luo, G.,
578 and Kump, L.R., 2014, Early Triassic seawater sulfate drawdown: Geochimica et Cosmochimica
579 Acta, v. 128, p. 95-113.
580 Walter, M.R., Veevers, J.J., Calver, C.R., Gorjan, P., and Hill, A.C., 2000, Dating the 840-544 Ma
581 Neoproterozoic interval by isotopes of strontium, carbon, and sulfur in seawater, and some
582 interpretative models: Precambrian Research, v. 100, p. 371-433.
583 Wang, X., Jiang, G., Shi, X., and Xiao, S., 2016, Paired carbonate and organic carbon isotope variations
584 of the Ediacaran Doushantuo Formation from an upper slope section at Siduping, South China:
585 Precambrian Research, v. 273, p. 53-66.
586 Wilkin, R.T., and Barnes, H.L., 1996, Pyrite formation by reactions of iron monosulfides with dissolved
587 inorganic and organic sulfur species: Geochimica et Cosmochimica Acta, v. 60, p. 4167-4179.
588 Xiao, S., and Laflamme, M., 2009, On the eve of animal radiation: phylogeny, ecology and evolution of
589 the Ediacara biota: Trends in Ecology & Evolution, v. 24, p. 31-40.
590 Xiao, S., Muscente A.D., Chen, L., Zhou, C., Schiffbauer, J.D., Wood, A.D., Polys, N.F., and Yuan, X.,
591 2014, The Weng'an biota and the Ediacaran radiation of multicellular eukaryotes: National Science
592 Review, v. 1, p. 498-520.
593 Xiao, S., Narbonne, G.M., Zhou, C., Laflamme, M., Grazhdankin, D.V., Moczydlowska-Vidal, M., and
594 Cui, H., 2016, Towards an Ediacaran Time Scale: Problems, Protocols, and Prospects: Episodes, v.
595 39, p. 540-555.
596 Yin, L., Zhu, M., Knoll, A.H., Yuan, X., Zhang, J., and Hu, J., 2007, Doushantuo embryos preserved
597 inside diapause egg cysts: Nature, v. 446, p. 661-663.
598 Yuan, X., Chen, Z., Xiao, S., Zhou, C., and Hua, H., 2011, An early Ediacaran assemblage of
599 macroscopic and morphologically differentiated eukaryotes: Nature, v. 470, p. 390-393.

600 Zaback, D.A., and Pratt, L.M., 1992, Isotopic composition and speciation of sulfur in the Miocene
601 Monterey Formation: reevaluation of sulfur reactions during early diagenesis in marine
602 environments: Geochimica et Cosmochimica Acta, v. 56, p. 763-774.
603 Zhang, S., Jiang, G., Zhang, J., Song, B., Kennedy, M.J., and Christie-Blick, N., 2005, U-Pb sensitive
604 high-resolution ion microprobe ages from the Doushantuo Formation in south China: Constraints on
605 late Neoproterozoic glaciations: Geology, v. 33, p. 473-476.
606 Zhang, S., Li, H., Jiang, G., Evans, D.A.D., Dong, J., Wu, H., Yang, T., Liu, P., and Xiao, Q., 2015, New
607 paleomagnetic results from the Ediacaran Doushantuo Formation in South China and their
608 paleogeographic implications: Precambrian Research, v. 259, p. 130-142.
609 Zhou, C., and Xiao, S., 2007, Ediacaran $\delta^{13}C$ chemostratigraphy of South China: Chemical Geology, v.
610 237, p. 89-108.
611 Zhou, C., Xie, G., McFadden, K., Xiao, S., and Yuan, X., 2007, The diversification and extinction of
612 Doushantuo-Pertatataka acritarchs in South China: causes and biostratigraphic significance:
613 Geological Journal, v. 42, p. 229-262.
614 Zhou, C., Xiao, S., Wang, W., Guan, C., Ouyang, Q., and Chen, Z., 2017, The stratigraphic complexity of
615 the middle Ediacaran carbon isotopic record in the Yangtze Gorges area, South China, and its
616 implications for the age and chemostratigraphic significance of the Shuram excursion: Precambrian
617 Research, v. 288, p. 23-38.
618 Zhu, M., Gehling, J.G., Xiao, S., Zhao, Y., and Droser, M.L., 2008, Eight-armed Ediacara fossil
619 preserved in contrasting taphonomic windows from China and Australia: Geology, v. 36, p. 867-870.
620 Zhu, M., Zhang, J., Steiner, M., Yang, A., Li, G., and Erdtmann, B., 2003, Sinian-Cambrian stratigraphic
621 framework for shallow- to deep-water environments of the Yangtze Platform: an integrated approach:
622 Progress in Natural Science, v. 13, p. 951-960.
623 Zhu, M., Zhang, J., and Yang, A., 2007, Integrated Ediacaran (Sinian) chronostratigraphy of South China:
624 Palaeogeography, Palaeoclimatology, Palaeoecology, v. 254, p. 7-61.
625 Zhu, M., Lu, M., Zhang, J., Zhao, F., Li, G., Yang, A., Zhao, X., and Zhao, M., 2013, Carbon isotope
626 chemostratigraphy and sedimentary facies evolution of the Ediacaran Doushantuo Formation in
627 western Hubei, South China: Precambrian Research, v. 225, p. 7-28.

628 **Supplementary Tables**

629 Table DR1: Carbon-sulfur geochemical data of the study sections [a]

630

Sample	Depth (m above Nantuo Fm.)	Estimated age (Ma)	TIC (wt. %)	$\delta^{13}C_{carb}$ (‰ VPDB)	$\delta^{34}S_{py}$ (‰ VCDT)	$\delta^{34}S_{CAS}$ (‰ VCDT)	$\Delta^{34}S_{CAS-Py}$ (‰ VCDT)	[CAS] (ppm in carbonate)
1. Jiulongwan Section (Inner shelf facies)								
HN-23	154	551	1.1	-5.3	-13.5			
HN-21	152	552.3	3.7	-4.4	-15.7	14.2	29.9	686.6
HN-20	151	552.9	1.0	-5.6		17.4		1390.1
HN-19	150	553.6	1.4	-6.6		16.7		794.2
HN-18	149	554.2	1.6	-6.4	-13.8	15.5	29.3	795.1
HN-17	148	554.9	1.3	-7.2		19.2		393.6
HN-16	147	555.5	0.5	-7.4				5064
HN-15	146	556.2	1.8	-7.9	-10.9	16.2	27.1	1026.7
HN-13	144	557.4	1.1	-7.8	-7.7			
HN-09	144	557.4	0.9	-8.3	-7.4			
HN-12	143	558.1	0.8	-7.8	-6.1			
HN-11	142.2	558.6	0.6	-6.4	-10.7			
JLW-01	142	558.7	10.4	-7.8	-13.4			422.2
HN-08	141.5	559	11.0	-8.6	-13.6	34.3	47.9	3263.9
JLW-02	141.3	559.2	10.5	-7.7				
HN-10	140.9	559.4	10.8	-8.7	-7.6			12.4
JLW-03	140.6	559.6	10.6	-7.7	-5.9	25.2	31.1	586.4
JLW-04	140.3	559.8	11.9	-7.5	-11.6	25.7	37.3	942.9
HN-06	140	560	10.6	-7.8	-8.0	29.7	37.7	118.9
JLW-05	139.9	560	9.5	-7.9				
JLW-06	139	560.3	10.7	-8.0	-8.0	19.7	27.7	1127.2
HN-07	138.5	560.4	10.8	-8.2	-6.9			
JLW-07	138.2	560.5	11.2	-8.5				
JLW-08	137.1	560.7	10.4	-8.4	-3.5	13.9	17.4	731.8
JLW-09	136	561	11.4	-8.3				
JLW-10	135	561.3		-8.4	-8.8	13.5	22.3	
JLW-11	134.2	561.5	10.5	-8.4				
JLW-12	133.6	561.6	10.1	-8.4	-16.2			283.3
JLW-13	132.7	561.8	11.1	-8.5				
JLW-14	132	562	11.4	-8.5	-13.6	15.8	29.4	264.6
JLW-15	131	562.3	11.1	-8.5				

JLW-16	130	562.5	10.1	-8.6		18.5		879.2
JLW-17	129	562.8	10.6	-8.7				
JLW-18	128.3	562.9	11.3	-8.8	4.7	18.4	13.7	844.7
JLW-19	127	563.3	12.2	-8.8				
JLW-20	126.2	563.5	10.8	-8.9				
JLW-21	125.2	563.7	10.1	-8.9	3.7	18.4	14.7	816.2
JLW-22	124.2	564	10.3	-8.7				
JLW-23	123.2	564.2	10.5	-9.0	-7.1	15.5	22.6	323.1
JLW-24	122	564.5	9.6	-9.0				
JLW-25	121.2	564.7	10.5	-9.0	14.2	20.2	6.0	409.5
JLW-26	120	565	10.2	-9.1	4.0			701.5
JLW-27	119.4	565.2	11.7	-9.1				
JLW-28	118.6	565.4	10.0	-9.1				
JLW-29	118	565.5	10.5	-9.0	0.2	14.6	14.4	602.9
JLW-30	117	565.8	10.5	-8.9				
JLW-31	116	566	11.1	-9.1	-4.8			
JLW-32	115	566.3	8.5	-8.7		21.3		969.1
JLW-33	114	566.5	10.1	-7.8	3.8	28.3	24.5	923.8
HN-05	113.3	566.7	10.3	-9.1	-2.9	20.8	23.7	
JLW-34	113	566.8	10.3	-6.3				
JLW-35	112	567	11.6	-5.4	-1.5	17.2	18.7	304.9
JLW-36	111	567.3	8.9	-6.4				
JLW-37	110.7	567.3	9.8	-6.1				
JLW-38	109.6	567.6	12.2	-5.1		26.3		
JLW-39	108.6	567.9	3.5	-2.0				
JLW-40	107.7	568.1	14.2	-2.7		19.9		447.8
JLW-41	106.6	568.4	11.7	-1.8				
JLW-42	105.6	568.6	11.6	-1.3	8.0	18.6	10.6	480.2
HN-04	105	568.8	9.6	-8.1	2.4			
JLW-43	104.6	568.9	10.2	-0.8	2.0	28.3		
JLW-44	103.7	569.1	11.2	-0.2				
JLW-45	102.7	569.3	12.0	-0.1				
JLW-46	101.7	569.6	10.4	2.7				615.1
JLW-47	100.8	569.8	10.4	2.9				
JLW-48	99.8	570.1	12.0	2.9	0.6	29.9	29.3	
JLW-49	98.8	570.3	8.9	3.5				
HN-02	98	570.5	12.3	-2.7	-6.1			
JLW-50	97.8	570.6	11.2	2.6	-3.2	33.3	36.5	528.9
JLW-51	96.8	570.8	11.8	3.2	10.4			
JLW-52	95.8	571.1	11.1	4.0				
JLW-53	94.8	571.3		4.3				

JLW-54	93.8	571.6	9.2	4.5	30.0	36.4	6.4	422.1
JLW-55	92.8	571.8	10.8	4.8				
HN-01	92	572	11.8	0.3	11.5			
JLW-56	91.6	572.1	10.7	4.4		29.7		73.7
JLW-57	91	572.3	10.6	4.5				
SSFT-12.6	83.6	574.1			21.9	35.9	14.0	
SSFT-11.58	82.9	574.3			20.1			
SSFT-9.8	80.8	574.8			30.2			
SSFT-9.0	80	575			29.8	39.0	9.2	
2. Siduping Section (Upper slope facies)								
SDP-154	166.1	551	0		3.3			
SDP-155	165.9	551.1	0.18		3.9			
SDP-156	165.5	551.2	0		5.0			
SDP-159	164.9	551.5	0		14.1			
SDP-161	163.7	551.9	0.01		-0.6			
SDP-163	162.9	552.3	3.03		9.7			
SDP-164	162.3	552.5	0		-5.9			
SDP-166	161.7	552.8	0.28		1.6			
SDP-167	161.4	552.9	0.06		2.5			
SDP-168	161.1	553	0.21		-1.2			
SDP-169	161	553	13.2	-8.0				
SDP-170	160.7	553.1		-8.3	-4.3			
SDP-171	160.4	553.3	12.32	-2.2				
SDP-172	160.1	553.4	10.72	-1.7	3.8	6.3	2.5	147
SDP-173	159.9	553.5	11.27	-2.0				
SDP-174	159.6	553.6	7.29	-1.4	2.3	6.9	4.6	169.5
SDP-175	159.4	553.7	10.33	-2.6				
SDP-177	159	553.8	4.04	0.1	-0.6			
SDP-178	158.6	554	11.18	-2.4	1.5	5.1	3.6	82
SDP-179	158.3	554.1	12.05	-2.9	8.3			
SDP-180	157.9	554.3	10.25	-4.9	5.5	7.2	1.7	92.8
SDP-181	157.4	554.5	12.24	-2.4	7.8	10.6	2.8	32.6
SDP-182	157.2	554.6	13.3	-5.3				
SDP-183	156.6	554.8	11.37	-5.7	4.8	9.5	4.7	19.2
SDP-184	156.2	554.9	9.89	-5.7				
SDP-185	156	555			3.5			
SDP-186	155.8	555.1	0		-7.1			
SDP-188	155.6	555.2	0		-8.6			
SDP-191	155.2	555.3	2.8		-0.6	27.4	28.0	726
SDP-192	155	555.4	12.48	-6.2				

SDP-193	154.5	555.6	1.72	-5.2	-6.0			
SDP-194	154.1	555.8	11.1	-5.5				
SDP-195	152.8	556.3	11.49	-7.3	-0.4			
SDP-197	150.7	557.1	11.34	-5.4	-6.2	16.1	22.3	93.4
SDP-198	150.2	557.3	10.07	-4.7				
SDP-199	149.4	557.7	11.61	-3.1				
SDP-200	148.4	558.1	11.62	-3.2	-10.9	0.7	11.6	71.2
SDP-201	148	558.2	4.01	-3.9				
SDP-202	146	559	7.74	-3.6				
SDP-215	145	559.4	11.49	1.0				
SDP-214	144	559.8	9.86	1.9	15.5	26.3	10.8	21.0
SDP-213	143	560.2	9.32	2.4				
SDP-212	142	560.4	9.17	2.2	9.4	23.8	14.4	74.1
SDP-211	139.5	561	9.96	1.9	7.6	40.5	32.9	157.8
SDP-210	136.7	561.6	12.62	1.0				
SDP-209	134.2	562.1	9.18	1.7		47.6		39.1
SDP-208	132.8	562.4	10.13	1.8				
SDP-206	128	563.4	12.26	-2.1				
SDP-205	124	564.3	11.97		7.4	13.6	6.2	35.7
SDP-204	123.5	564.4	11.54		4.2			
SDP-203	122.7	564.5	11.11	1.2	5.2	14.6	9.4	93.2
SDP-143	114.7	566.2	8.6	1.6	13.7			
SDP-142	114.1	566.4	8.0	1.7	3.3			
SDP-140	113.2	566.6	7.6	2.1	35.6			
SDP-138	111.7	566.9	8.2	2.3	10.7	22.9	12.2	169.8
SDP-135	110.5	567.1	9.6	2.6	21.0			
SDP-134	109.8	567.3	6.9	0.9	12.9			352.1
SDP-133	108.6	567.5	7.2	1.7	13.8			
SDP-131	108.4	567.6	8.2	1.4	14.1	24.3	10.2	306.9
SDP-130	108	567.7	8.0	0.5				
SDP-129	107.4	567.8	7.8	1.7	19.9	27.1	7.2	309
SDP-128	106.7	567.9	7.1	1.9	13.1			
SDP-126	106	568.1	8.2	2.1	14.9	26.2	11.4	285.6
SDP-125	105.1	568.3	6.9	2.0	12.2			
SDP-124	104.7	568.4	7.4	2.5	7.2			
SDP-123	104.2	568.5	7.4	2.3	16.4			
SDP-122	103.2	568.7	8.9	2.6	11.1	25.9	14.8	193
SDP-121	103	568.7	8.2	2.9	14.1			
SDP-120	102.2	568.9	6.7	1.9	18.7			
SDP-119	101.3	569.1	7.5	1.5	14.6			
SDP-118	100.5	569.3	8.3	2.3	10.3	21.4	11.0	119.5

SDP-117	99.5	569.5	9.7	0.9	10.4			
SDP-116	98.8	569.6	9.5	1.6	8.3	19.2	10.9	411.1
SDP-114	97.7	569.9	9.4	1.8	20.0			
SDP-111	96.4	570.1	7.6	1.7		27.3		593.1
SDP-110	96.1	570.2	8.6	2.1	5.3			
SDP-108	93.3	570.8	10.5	1.8	17.6			93.9
SDP-106	92.1	571	9.6	1.5	21.2			
SDP-103	90.7	571.3	8.7	2.1	20.0	26.7	6.8	231.3
SDP-101	89.7	571.6	9.2	2.1	19.7			
SDP-99	89	571.7	8.7	2.2	19.8	29.0	9.3	232.9
SDP-97	87.7	572	7.7	1.2	13.3			
SDP-96	87	572.1	7.0	1.2	13.2	11.9	-1.3	284.1
SDP-95	86.2	572.3	7.7	1.8	11.2			
SDP-94	85.4	572.5	10.8	0.1		19.7		117.7
SDP-92	84.5	572.7	8.4	1.4	17.5			
SDP-91	84	572.8	10.8	1.2	22.2	26.3	4.0	84.8
SDP-89	82.7	573	9.7	2.7	28.8			
SDP-88	81.9	573.2	10.4	4.0		23.5		94.0
SDP-86	80.7	573.5	8.9	4.3	30.9			
SDP-84	79.2	573.8	9.6	4.5	32.5	24.3	-8.2	87.0
SDP-83	78.6	573.9	6.9	4.3	28.2			
SDP-82	77.6	574.1	8.7	4.4	29.1	19.2	-9.9	111.2
SDP-81	76.8	574.3	11.4	4.5	30.8			
SDP-80	75.4	574.6	8.5	4.7	34.6	25.5	-9.1	
SDP-78	74.2	574.9	8.6	4.6	28.1			
SDP-76	73.5	575	11.7	4.6	32.1			

Notes:

[a] All C-S isotope and [CAS] data of Jiulongwan (JLW) and Siduping (SDP) samples are from this study, Li et al. (2010, 2017), whereas data for SSFT-labeled samples are from McFadden et al. (2008).

Table DR2: Sulfur chemostratigraphic comparison in stages between inner-shelf Jiulongwan (JLW) and upper-slope Siduping (SDP) sections

JLW		EP2	EN3a	EN3b		EN3c
				EN3b-1	EN3b-2	
$\delta^{34}S_{py}$ [a]	(‰)	23.9±7.5 (6)	0.8±5.2 (11)	-2.7±9.9 (10)	-9.5±2.8 (12)	-10.7±2 (4)
$\delta^{34}S_{CAS}$ [a]	(‰)	35.3±3.9 (4)	24.4±5.5 (10)	16.5±2.4 (9)	26.9±4.1 (5)	16.5±1.7 (6)
$\Delta^{34}S_{CAS\text{-}py}$ [a]	(‰)	9.9±3.8 (3)	23.9±8.9 (6)	17.6±7.1 (8)	36.3±4.9 (5)	28.8±1.5 (3)
[CAS] [b]	(ppm)	248 (129-366)	529 (442-926)	652 (301-832)	586 (115-1203)	795 (675-1537)

SDP		EP2	EN3a	EN3b		EN3c	
				EN3b-1	EN3b-2	EN3c-1	EN3c-2
$\delta^{34}S_{py}$ [a]	(‰)	30.6±2.2 (9)	15.5±4.4 (5)	14.1±6.6 (31)	10.8±4.1 (3)	-4.5±4.2 (8)	3.2±3.1 (18)
$\delta^{34}S_{CAS}$ [a]	(‰)	23.2±2.7 (4)	19.3±7.2 (3)	23.2±5.1 (12)	34.5±11.4 (4)	14.7±13.4 (3)	7.6±2.0 (6)
$\Delta^{34}S_{CAS\text{-}py}$ [a]	(‰)	-9.1±0.9 (3)	1.4±3.7 (2)	9.9±2.6 (11)	19.4±11.9 (3)	20.6±8.3 (3)	3.3±1.2 (6)
[CAS] [b]	(ppm)	94 (89-106)	118 (95-231)	232 (96-349)	57 (30-118)	93 (78-524)	87 (30-152)

Notes:

[a] Data are given as mean±1σ (n).

[b] Data are given as median (16^{th}-84^{th} percentiles).

Table DR3: $[SO_4^{2-}]_{SW}$ modeled for the Shuram Excursion at each study section

JLW section		**Age** [a] (Ma)	**Depth** (m)	**Sed. Rate** [b] (m Myr^{-1})	$\Delta^{34}S_{sulfate\text{-}py}$ (‰)		$\partial^{34}S_{CAS}/\partial t$ (‰ Myr^{-1})		$[SO_4^{2-}]_{SW}$ [c] (mM)		
					Avg.	Max.	Avg.	Max.	Min.	Avg.	Max.
EN3c		560-551	142-154	1.56	28.8	29.9	3.2	5.8	11.0 [d]	20.0 [d]	20.7 [d]
EN3b	3b-2	575-560	135-142	4.0	36.4	47.9	19.8	40.0	2.0	4.1	5.4
	3b-1		115-135		17.6	29.4	4.5	9.4	4.2	8.7	14.5
EN3a			93-115		23.9	36.5	12.8	28.0	1.9	4.1	6.3
EP2			80-93		9.9	14.0	6.2	12.2	1.8	3.5	5.0
SDP section		**Age** [a] (Ma)	**Depth** (m)	**Sed. Rate** [b] (m Myr^{-1})	$\Delta^{34}S_{sulfate\text{-}py}$ (‰)		$\partial^{34}S_{CAS}/\partial t$ (‰ Myr^{-1})		$[SO_4^{2-}]_{SW}$ [c] (mM)		
					Avg.	Max.	Avg.	Max.	Min.	Avg.	Max.
EN3c	3c-2	560-551	158-166	2.5	3.3	4.7	7.1	16.9	0.4	1.0	1.5
	3c-1		143-158		20.6	28.0	11.5	16.8	2.7	4.0	5.4
EN3b	3b-2	575-560	128-143	4.7	19.4	32.9	13.9	31.3	1.4	3.1	5.3
	3b-1		87-128		9.9	14.8	5.6	15.9	1.4	3.9	5.9
EN3a			80-87		4.0	4.0	22.4	22.7	0.4		0.4
EP2			73-80		-9.1	-8.2	—		0.0 [e]		

Notes:

[a] Based on sequence stratigraphic correlation, we used the ages of ca. 575 Ma (disappearance of definitive mobile bilaterians; Narbonne, 2005; Xiao and Laflamme, 2009; Chen et al., 2014; Droser and Gehling, 2015), ca. 560 Ma (base of Doushantuo Member IV (i.e., Miaohe Member); Kendall et al., 2015), and ca. 551 Ma (top of the Doushantuo Member IV; Condon et al., 2005; Zhang et al., 2005) as anchors to constrain the age of individual data points from the South China sections.

[b] Sedimentation rate for each study unit is based on its thickness and duration.

[c] Based on methods developed in Algeo et al. (2015).

[d] $\partial^{34}S$ data from Li et al. (2010) are for reference only, as TIC < 3 %.

[e] All $\Delta^{34}S_{sulfate\text{-}py}$ in EP2 at SDP are < 0 ‰, implying $[SO_4^{2-}]_{sw}$ close to zero.

Table DR4: Elemental concentration data used for S-isotope data quality evaluation in this study [a]

Sample	Fe_T	Ca	Mg	S_{py}
	(wt. %)	(wt. %)	(wt. %)	(wt. %)
Jiulongwan Section (Inner shelf facies)				
HN-23	3.3	2.7	2.0	2.3
HN-21	2.7	6.0	3.9	1.2
HN-20				
HN-19				
HN-18	2.3	3.3	2.4	1.1
HN-17				
HN-16				
HN-15	2.7	2.1	1.9	1.6
HN-13	2.9	3.5	2.5	1.2
HN-09	2.8	2.0	1.8	2.3
HN-12	3.1	1.8	1.6	2.5
HN-11	3.2	1.6	1.4	2.5
JLW-01	1.0	19.5	8.6	1.0
HN-08	0.5			0.3
JLW-02				
HN-10	0.7	26.8	6.0	0.4
JLW-03	0.9	22.4	8.0	0.9
JLW-04				0.4
HN-06	0.8			0.4
JLW-05	0.8	22.0	7.8	
JLW-06	0.6	28.4	5.9	0.4
HN-07	0.7	25.4	5.8	0.3

JLW-07	0.3	37.2	0.8	
JLW-08	0.4			0.4
JLW-09	0.3	37.7	0.4	
JLW-10	0.4	38.7	0.5	0.3
JLW-11	0.7	31.4	2.3	
JLW-12				0.3
JLW-13	0.6	38.4	0.6	
JLW-14	0.3	37.7	0.4	0.1
JLW-15				
JLW-16				0.0
JLW-17	0.4	37.9	0.4	
JLW-18	0.3	37.8	0.4	0.1
JLW-19	0.5	35.7	0.9	
JLW-20				
JLW-21				0.2
JLW-22				
JLW-23	0.4	37.2	0.6	0.3
JLW-24				
JLW-25				0.3
JLW-26	0.5	33.6	0.9	0.4
JLW-27				
JLW-28	0.7	30.4	2.1	
JLW-29	0.4	34.6	0.7	0.3
JLW-30	1.0	19.7	10.3	
JLW-31	0.8	20.8	9.6	0.0
JLW-32	1.0	19.4	10.1	
JLW-33	0.7	19.3	10.0	0.0
HN-05	0.6			0.3
JLW-34	0.8	19.3	10.3	
JLW-35	0.6	20.8	11.0	0.0
JLW-36	1.0	19.3	10.2	
JLW-37	1.1	18.0	9.5	
JLW-38	0.1	22.0	10.7	0.0
JLW-39				
JLW-40	0.2	21.2	10.3	0.0
JLW-41				
JLW-42	0.3	21.0	10.2	
HN-04	0.3	17.3	7.9	0.6
JLW-43				
JLW-44	0.6	19.5	9.6	0.0
JLW-45				

JLW-46				
JLW-47				
JLW-48	0.3	20.8	9.8	0.0
JLW-49				
HN-02	0.4	20.4	9.9	0.0
JLW-50				0.0
JLW-51				
JLW-52				
JLW-53				
JLW-54		19.6	9.5	0.0
JLW-55	0.1			0.0
HN-01	0.2	37.6	1.0	
JLW-56	0.1	19.5	10.4	
JLW-57	0.2	20.6	11.0	
Siduping Section (Upper slope facies)				
SDP-154	2.9	0.0	0.2	2.8
SDP-155	3.7	0.1	0.4	2.8
SDP-156		0.1	0.4	3.2
SDP-159	1.1	0.0	0.3	0.0
SDP-161	0.9	0.0	0.2	0.4
SDP-163	1.1	0.8	0.2	0.0
SDP-164				0.0
SDP-166	0.1	0.6	0.3	0.1
SDP-167	2.6	0.0	0.6	2.6
SDP-168				6.4
SDP-169				
SDP-170	4.1	10.1	5.3	5.2
SDP-171				
SDP-172				2.1
SDP-173	1.3	16.7	8.2	
SDP-174	2.1	12.2	6.5	2.6
SDP-175				
SDP-177				4.0
SDP-178	0.9	17.0	8.3	1.1
SDP-179	0.3	19.6	9.2	0.0
SDP-180				1.0
SDP-181				0.1
SDP-182	0.2	19.8	9.4	
SDP-183				0.8
SDP-184	0.9	15.9	7.8	

SDP-185	4.0	0.6	0.8	4.8
SDP-186				2.9
SDP-188	3.5			3.1
SDP-191	0.2			3.3
SDP-192		19.7	9.1	
SDP-193	0.2	2.9	1.8	0.1
SDP-194	2.1	0.0	0.8	0.0
SDP-195				0.6
SDP-197				0.6
SDP-198				
SDP-199	0.0	7.4	4.2	
SDP-200				0.9
SDP-201	0.0	6.7	3.9	
SDP-202	0.1	12.8	6.7	0.0
SDP-215				
SDP-214				0.0
SDP-213				
SDP-212	0.8	15.5	9.3	0.0
SDP-211				0.1
SDP-210	0.1	19.7	9.6	0.0
SDP-209				0.0
SDP-208	0.6	16.6	9.7	0.0
SDP-206	0.0	20.5	9.8	0.0
SDP-205				0.2
SDP-204	0.4	18.7	9.5	0.4
SDP-203				0.5
SDP-143				
SDP-142	1.0	13.3	9.1	0.0
SDP-140				0.3
SDP-138	0.8	14.0	8.6	0.0
SDP-135				0.2
SDP-134	2.0	11.6	8.6	0.4
SDP-133				
SDP-131	1.2	14.2	9.0	1.3
SDP-130				0.5
SDP-129	1.5	13.1	8.9	0.8
SDP-128				0.6
SDP-126	1.5	13.7	8.9	0.6
SDP-125				0.7
SDP-124	1.6	12.4	8.6	0.5
SDP-123				0.1

SDP-122	1.1	15.1	9.2	0.4
SDP-121				0.2
SDP-120	1.6	11.9	8.9	0.4
SDP-119				0.5
SDP-118				0.5
SDP-117				0.3
SDP-116	0.8	16.9	9.8	0.3
SDP-114				0.4
SDP-111	1.4	13.5	9.7	0.5
SDP-110				0.4
SDP-108	0.4	17.8	10.1	0.1
SDP-106				0.3
SDP-103	1.0	14.6	7.3	0.4
SDP-101				0.5
SDP-99	0.6	15.3	9.9	0.4
SDP-97				0.7
SDP-96	0.9	11.9	9.6	0.9
SDP-95				0.9
SDP-94	0.1	17.0	11.0	
SDP-92				0.0
SDP-91				0.0
SDP-89				0.0
SDP-88				0.0
SDP-86				0.0
SDP-84	0.1	17.0	11.0	0.0
SDP-83				0.0
SDP-82	0.1	15.1	11.2	
SDP-81	0.1			0.0
SDP-80				0.0
SDP-78				0.0
SDP-76				0.0

Notes:

[a] Data for samples labeled with "HN" are from Li et al. (2010).

666 Table DR5: Results of age sensitivity analyses for Jiulongwan (JLW) and Siduping (SDP)

667 sections.

JLW(Ma) EN3b-2	Accumulation rate (m/Myr)	$d\delta^{34}S_{CAS}/dt$ (avg. ‰/Myr)	$[SO_4^{2-}]_{SW}$ (mM)
-1 (574)	4.3	20	3.9
+1 (576)	3.75	17.6	4.6
-5 (570)	6	23.5	3.4
+5 (580)	3	15.7	5.1
-10 (565)	12	39	2
+10 (585)	2.4	14	5.7
JLW(Ma) EN3b-1	**Accumulation rate (m/Myr)**	**$d\delta^{34}S_{CAS}/dt$ (avg. ‰/Myr)**	**$[SO_4^{2-}]_{SW}$ (mM)**
-1 (574)	4.3	5.4	7.2
+1 (576)	3.75	4.3	9.1
-5 (570)	6	7.6	5.1
+5 (580)	3	3.8	10.2
-10 (565)	12	15.2	2.6
+10 (585)	2.4	3	13
JLW(Ma) EN3a	**Accumulation rate (m/Myr)**	**$d\delta^{34}S_{CAS}/dt$ (avg. ‰/Myr)**	**$[SO_4^{2-}]_{SW}$ (mM)**
-1 (574)	4.3	13.3	3.9
+1 (576)	3.75	10.7	4.9
-5 (570)	6	17.2	3.1
+5 (580)	3	8.6	6.1
-10 (565)	12	34.3	1.5
+10 (585)	2.4	6.9	7.6
JLW(Ma) EP2	**Accumulation rate (m/Myr)**	**$d\delta^{34}S_{CAS}/dt$ (avg. ‰/Myr)**	**$[SO_4^{2-}]_{SW}$ (mM)**
-1 (574)	4.3	6.7	3.3
+1 (576)	3.75	5.85	3.7
-5 (570)	6	9.4	2.3
+5 (580)	3	4.7	4.6
-10 (565)	12	18.7	1.2
+10 (585)	2.4	3.75	5.8

668

SDP (Ma) EN3c-2	Accumulation rate (m/Myr)	$d\delta^{34}S_{CAS}/dt$ (avg. ‰/Myr)	$[SO_4^{2-}]_{SW}$ (mM)
-1 (559)	2.9	8.2	0.9

+1 (561)	2.3	6.5	1.1
-5 (555)	5.75	16.3	0.5
+5 (565)	1.64	4.7	1.5
SDP (Ma) EN3c-1	**Accumulation rate (m/Myr)**	**$d\delta^{34}S_{CAS}/dt$ (avg. ‰/Myr)**	**$[SO_4^{2-}]_{SW}$ (mM)**
-1 (559)	2.9	13.3	3.4
+1 (561)	2.3	10.6	4.3
-5 (555)	5.75	26.5	1.8
+5 (565)	1.64	7.6	6
SDP (Ma) EN3b-2	**Accumulation rate (m/Myr)**	**$d\delta^{34}S_{CAS}/dt$ (avg. ‰/Myr)**	**$[SO_4^{2-}]_{SW}$ (mM)**
-1 (574)	5	15.2	2.8
+1 (576)	4.4	13.6	3.2
-5 (570)	7	20.9	2.1
+5 (580)	3.5	10.9	3.9
-10 (565)	14	40	1.1
+10 (585)	2.8	8.9	4.8
SDP (Ma) EN3b-1	**Accumulation rate (m/Myr)**	**$d\delta^{34}S_{CAS}/dt$ (avg. ‰/Myr)**	**$[SO_4^{2-}]_{SW}$ (mM)**
-1 (574)	5	6	3.7
+1 (576)	4.4	5.3	4.1
-5 (570)	7	8.3	2.6
+5 (580)	3.5	4.2	5.2
-10 (565)	14	16.7	1.3
+10 (585)	2.8	3.4	6.4
SDP (Ma) EN3a	**Accumulation rate (m/Myr)**	**$d\delta^{34}S_{CAS}/dt$ (avg. ‰/Myr)**	**$[SO_4^{2-}]_{SW}$ (mM)**
-1 (574)	5	23.8	0.4
+1 (576)	4.4	21	0.4
-5 (570)	7	33.4	0.3
+5 (580)	3.5	16.7	0.5
-10 (565)	14	66	0.15
+10 (585)	2.8	13.4	0.65

669

670 Table DR6: Modeling results of oceanic sulfate residence time

Mean oceanic SO_4^{2-} reservoir (times of modern level) or (mM)	**Riverine sulfate flux (times of modern level)**	**Residence time (years)**
1/15 or 2	400	2000
1/30 or 1	200	2000

1/50 or 0.6	120	2000
1/100 or 0.3	60	2000
1/300 or 0.1	20	2000

Supplementary Figures

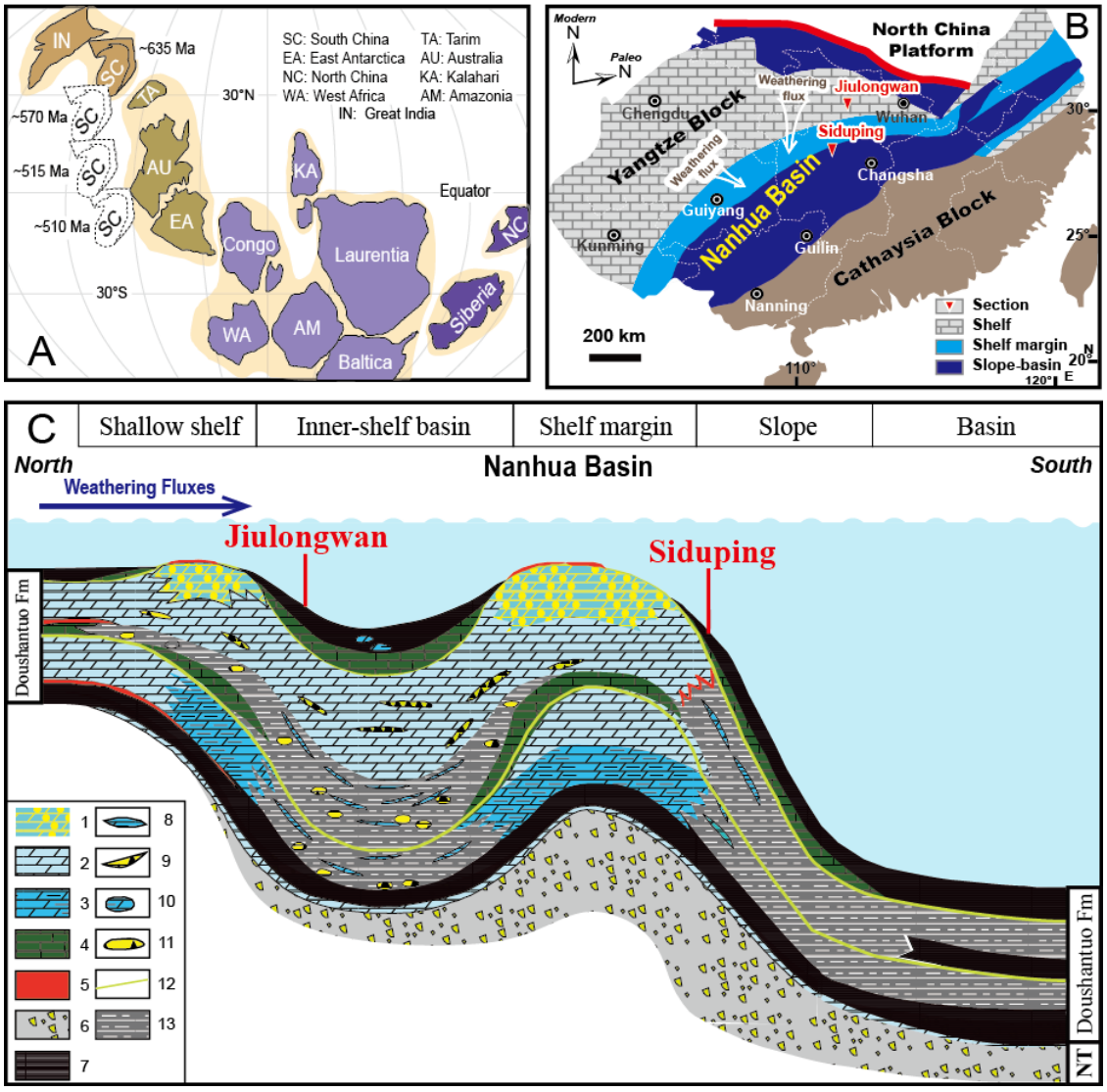

Figure DR1: Geological setting of the Ediacaran Doushantuo Formation in South China. (A) Ediacaran global paleogeography (modified from Zhang et al., 2015). (B) Palaeogeographic map of the Yangtze Platform during Doushantuo deposition (modified from Jiang et al., 2011) with the two study sections (Jiulongwan and Siduping) marked. (C) Proximal-to-distal transect across the Yangtze Platform, showing relative paleodepths of the study sections (after Zhu et al., 2013). Legend: 1, thick-bedded grainstone; 2, micritic dolostone; 3, muddy or silty laminated dolostone; 4, limestone; 5, phosphorite; 6, glacigenic diamictite; 7, black shale; 8, cherty bands and nodules in carbonate; 9, carbonate interbeds or lenticular beds; 10, cherty nodules in shale; 11, carbonate concretions; 12, sequence boundary; 13, dark or dark-gray silty shale or mudstone.

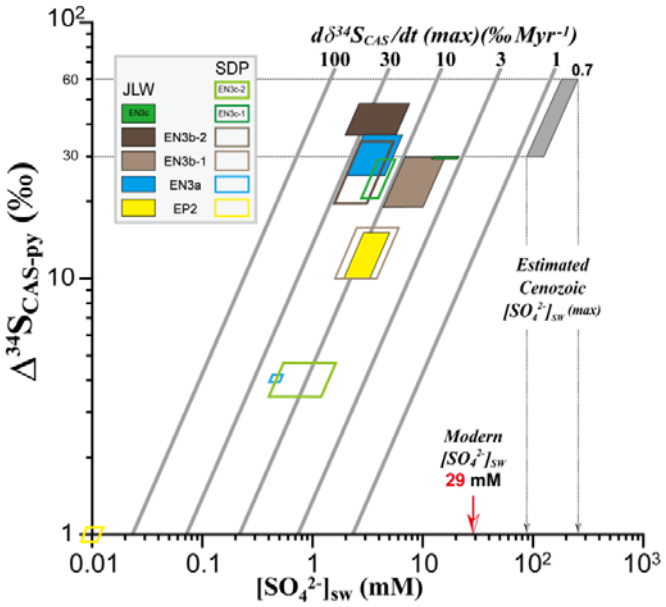

683

684

685 Figure DR2: Estimation of $[SO_4^{2-}]_{sw}$ for individual units of the Jiulongwan (JLW) and
686 Siduping (SDP) sections during the Shuram Excursion, based on the 'rate method' of Algeo
687 et al. (2015). The parallelograms represent measured values of $\partial\delta^{34}S_{CAS}/\partial t$(max), i.e., the
688 maximum rate of change of $\delta^{34}S_{CAS}$, and $\Delta^{34}S_{CAS\text{-}py}$, i.e., fractionation of S isotopes between
689 CAS and pyrite. The median and range of $[SO_4^{2-}]_{sw}$ estimates are read by projecting values
690 from the parallelograms to the abscissa. As an example, the light gray parallelogram
691 represents values for Cenozoic marine CAS, which yields $[SO_4^{2-}]_{sw}$ estimates that are only
692 slightly higher than the modern $[SO_4^{2-}]_{sw}$ of ~29 mM (Millero, 2005).

693

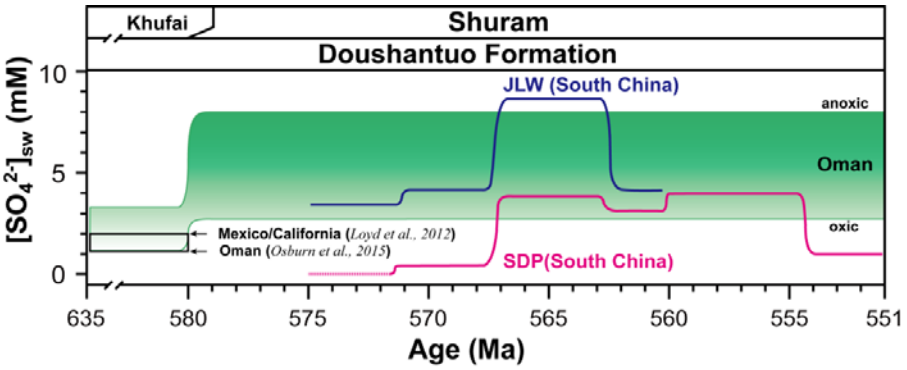

694

695 Figure DR3: A rough estimation of shelf marine sulfate concentrations during the Shuram
696 Excursion in Oman (green band) using "rate method" in this study. The origin sulfur isotope
697 dataset of Oman Khufai-Shuram Formation for modeling are from Fike et al. (2006). The
698 upper boundary of green band corresponds to a pyrite burial flux equal to 10×10^{13} g yr^{-1}
699 when the ocean was completely anoxic; the lower boundary of green band corresponds to a
700 pyrite burial flux equal to 4×10^{13} g yr^{-1} when the ocean was oxic; the black box reflects two
701 estimations of marine sulfate concentrations during per-Shuram period, which are from
702 Loyd et al. (2012) (<2 mM for USA) and Osburn et al. (2015) (<1.2 mM for Oman),
703 respectively. The modeling results of JLW (blue line) and SDP (carmine line) in South
704 China are provided for comparison.

705

706
707

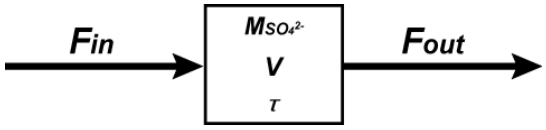

708
709

710 Figure DR4: A simple linear response system model for evaluating sulfate concentrations in
711 marine systems. F_{in} is riverine sulfate flux into the ocean, and F_{out} is the sedimentary sink
712 flux. M is oceanic sulfate mass, V is seawater volume, and τ is the seawater residence time
713 of sulfate.
714

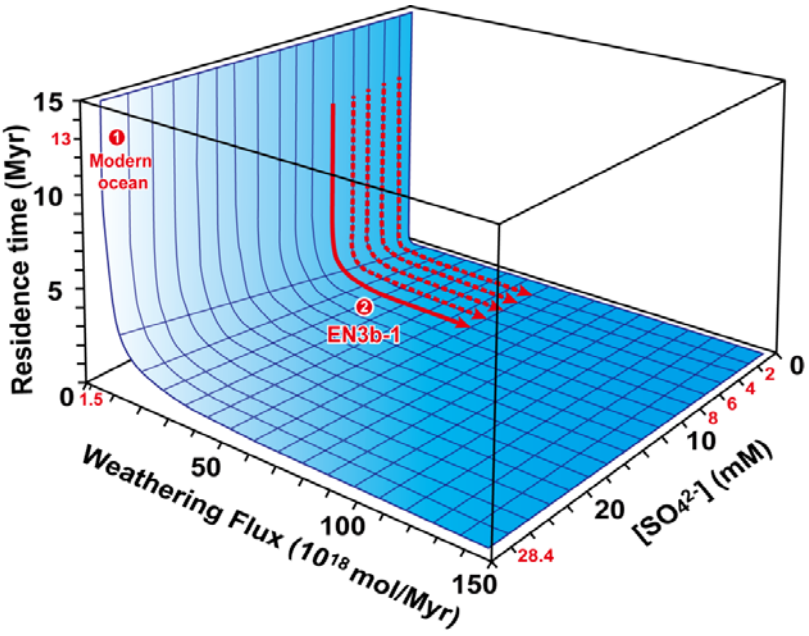

Figure DR5: A 3-D diagram showing the relationship between seawater sulfate concentrations ($[SO_4^{2-}]_{sw}$), sulfate weathering fluxes (F_{in}), and oceanic sulfate residence times (τ). Red circle 1 represents modern ocean conditions with $[SO_4^{2-}]_{sw}$ = 28.4 mM, F_{in} = 1.5×10^{18} mol Myr^{-1}, and τ = 13 Myr; red circle 2 and red trend lines represent the changes in τ accompanying increased F_{in} using four different estimates of $[SO_4^{2-}]_{sw}$ during SE EN3b-1.

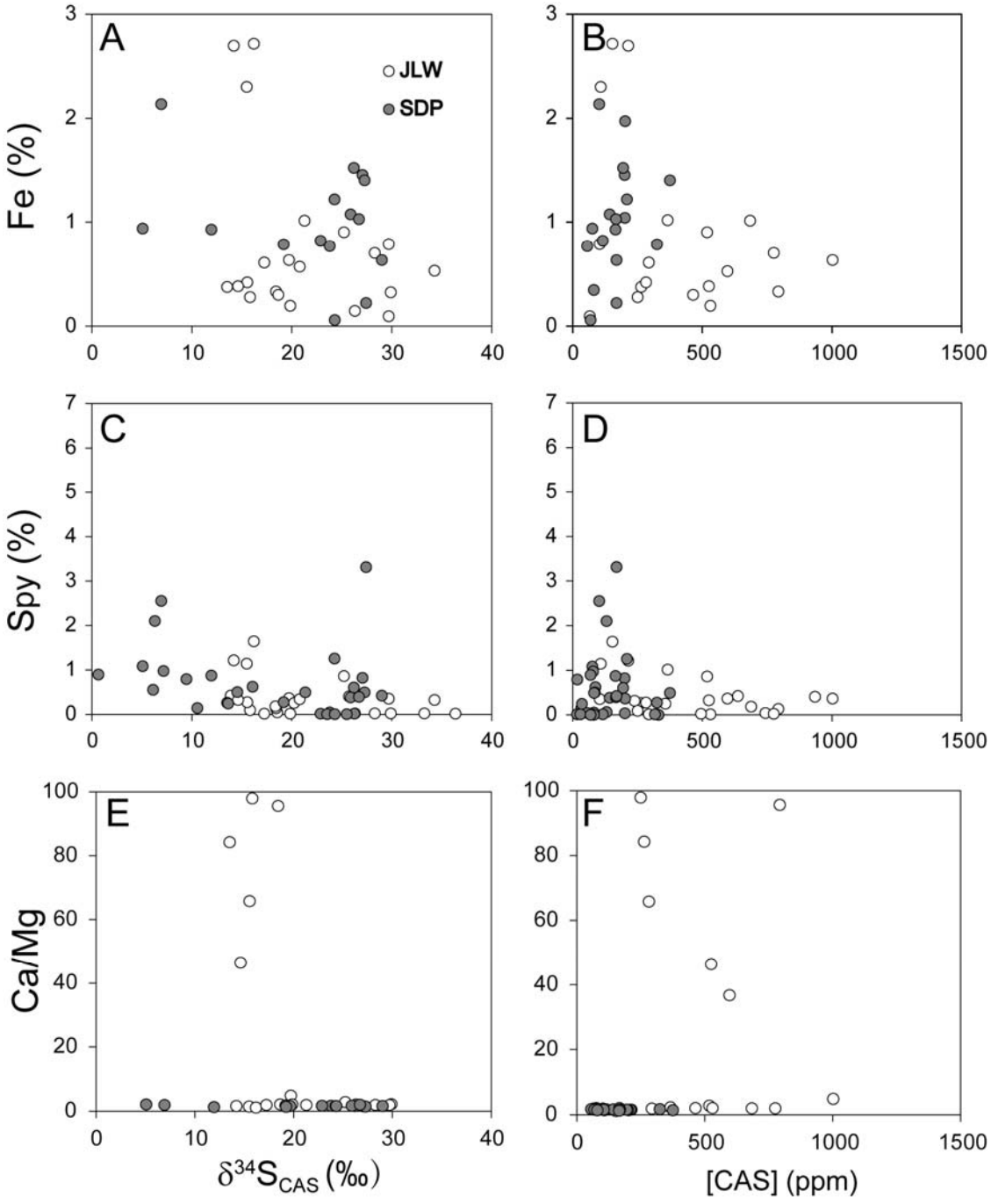

723

724 Figure DR6: Crossplots of $\delta^{34}S_{CAS}$ versus (A) total Fe (Fe_T), (C) pyrite sulfur (S_{py}), and (E)

725 Ca/Mg, and of [CAS] versus (B) total Fe (Fe_T), (D) pyrite sulfur (S_{py}), and (F) Ca/Mg. JLW

726 = Jiulongwan and SDP = Siduping. All relationships yield $R^2 < 0.1$.

727

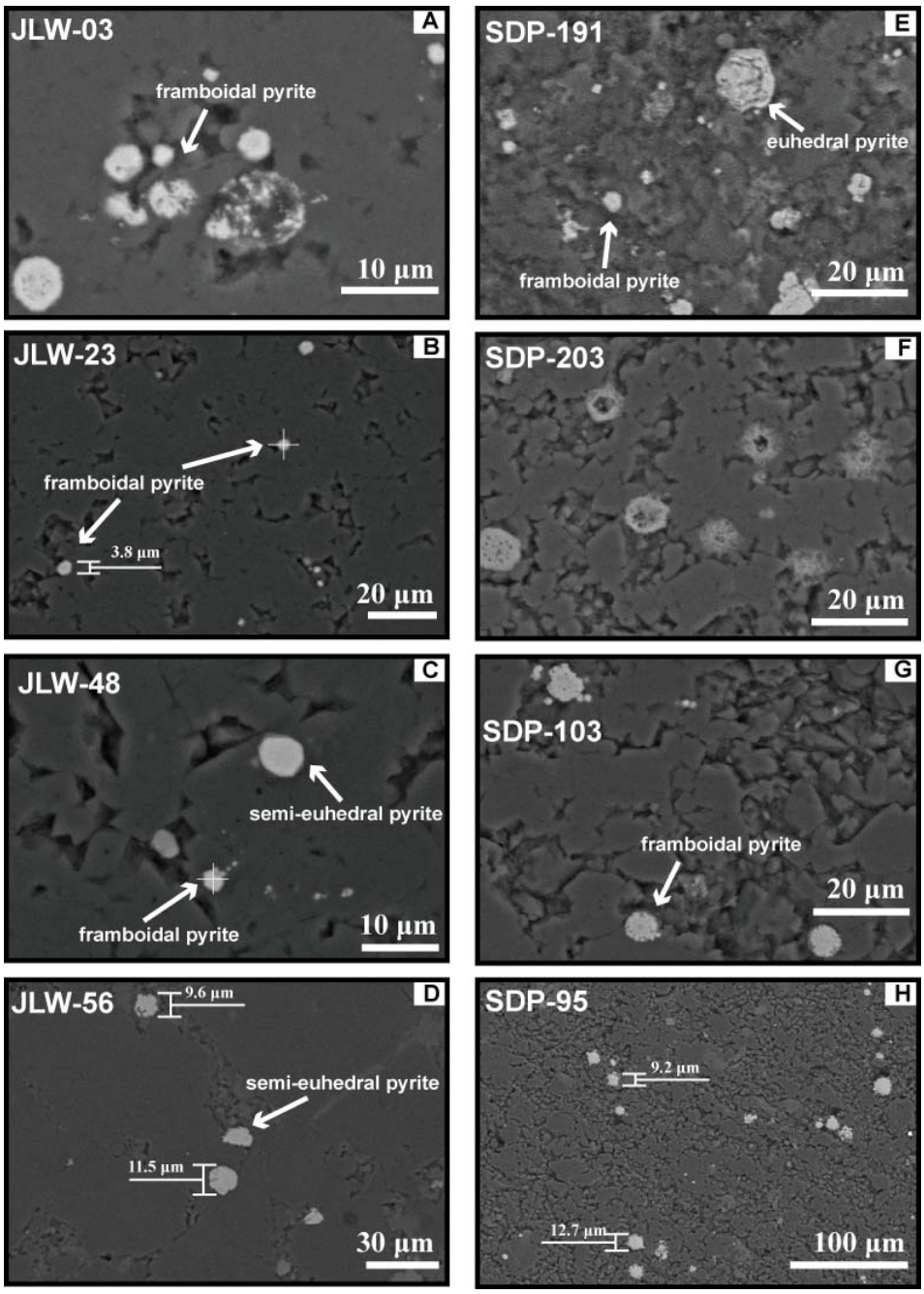

728

729

730 Figure DR7: Backscattered electron (BSE) images of typical pyrite framboids (A, B),
731 abundant framboids with a few euhedral crystals (C, D) in JLW samples, co-occurring
732 euhedral crystals with a few framboids (E) and typical pyrite framboids (F, G and H) in SDP
733 samples.

734

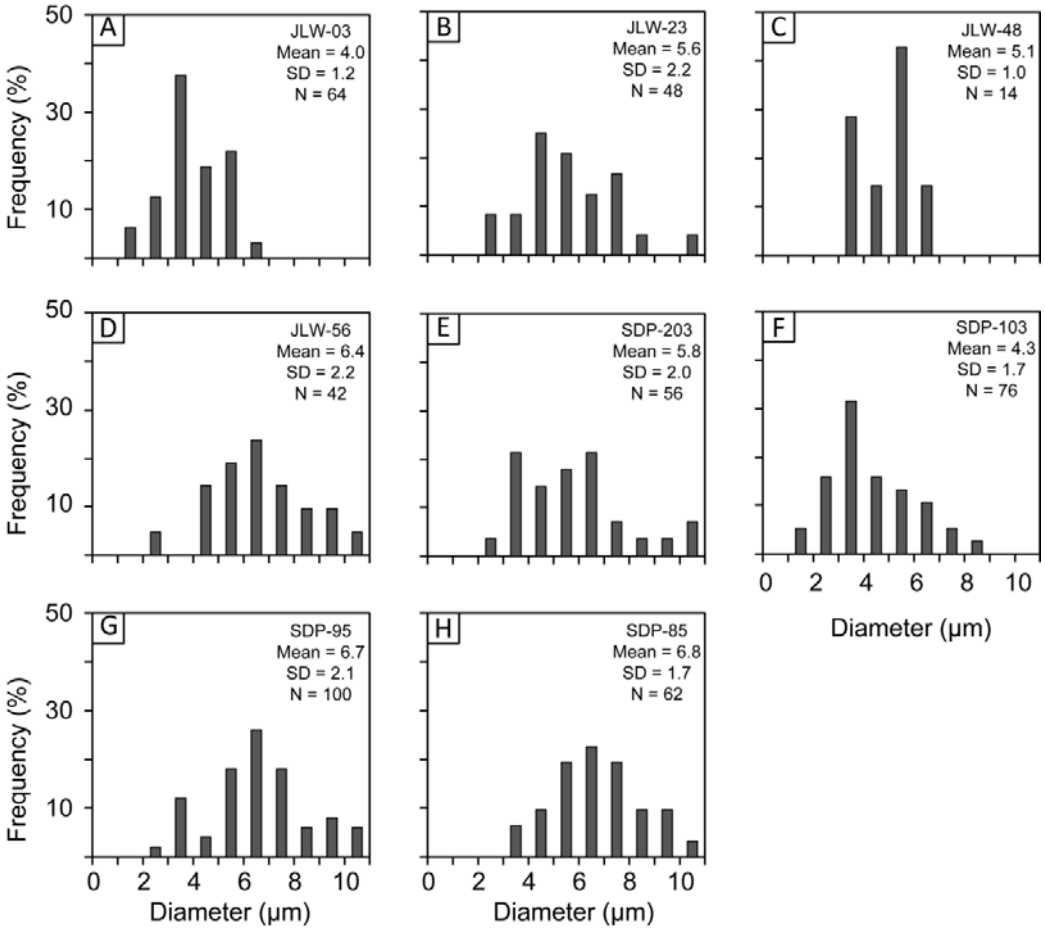

735

736

737 Figure DR8: Statistics of pyrite framboid size. A-D and E-H are for typical samples from

738 Jiulongwan (JLW) and Siduping (SDP) sections, respectively. SD = standard deviation.